Spatio-angular fluorescence microscopy I. Basic theory

TALON CHANDLER,[1,*] AUTHOR ORDER TBD,[2,*] AND PATRICK LA RIVIÈRE [1]

[1] *University of Chicago, Department of Radiology, Chicago, Illinois 60637, USA*
[2] *Publications Department, The Optical Society, 2010 Massachusetts Avenue NW, Washington, DC 20036, USA*
[3] *Currently with the Department of Electronic Journals, The Optical Society, 2010 Massachusetts Avenue NW, Washington, DC 20036, USA*
[*] *talonchandler@talonchandler.com*

Abstract: We introduce the basic elements of a spatio-angular theory of fluorescence microscopy. We start by modeling a microscope imaging an ensemble of in-focus fluorescent dipoles as a linear Hilbert-space operator with domain $\mathbb{L}_2(\mathbb{R}^2 \times \mathbb{S}^2)$ and range $\mathbb{L}_2(\mathbb{R}^2)$, and we express the operator in terms of four different sets of object-space basis functions. We show that the operator takes a particularly convenient form when expressed in a basis of spatial and spherical harmonics—a form we call the spatio-angular dipole transfer function. We demonstrate our formalism by analyzing a single-view paraxial epi-fluorescence microscope without using the monopole or scalar approximations. We show that this microscope has an angular band limit, and we demonstrate the value of the transfer function approach by efficiently simulating the imaging process with simple phantoms. Notably, we show that information about the out-of-plane orientation of ensembles of in-focus fluorophores is recorded by paraxial epi-fluorescence microscopes. We discuss the implications of our analysis for all quantitative fluorescence microscopy studies and lay out a path towards a complete theory.

1. Introduction

Fluorescence microscopes are widely used in the biological sciences for measuring the spatial distribution of fluorophores throughout a sample [cite]. While an unprocessed fluorescence micrograph reports the approximate distribution of fluorophores throughout a sample, all microscopes are diffraction limited [cite], so the image is a blurred version of the true fluorophore distribution.

Restoration techniques attempt to recover the true distribution of fluorophores using the measured data and a model of the imaging process. A model of the imaging process can be obtained theoretically (by mathematically modeling the instrument under idealized conditions), experimentally (by measuring the instrument's response to a known input), or by a combination of theory and experiment (by measuring parameters of an instrument model). In all cases the accuracy of the restored fluorophore distribution is limited by the accuracy of the imaging model. All theoretical imaging models make simplifying approximations that limit the accuracy of restorations, so it is important to verify that the approximations introduce an acceptable level of error. This work investigates the errors introduced by two common approximations in models of fluorescence microscopes—the *monopole approximation* and the *scalar approximation*.

The widely-used monopole model treats fluorophores as molecules that absorb and emit light isotropically. Despite their use in models, monopole absorber/emitters do not exist in nature. All real fluorophores absorb and emit light anisotropically, and in this work we investigate the more realistic dipole model of fluorophores. Since the absorption and emission patterns of many widely used fluorophores including green fluroescent protein (GFP) are known to be well described by the dipole model [cite Inoue], we start by considering the dipole model before higher-order multipole models.

The scalar approximation is another widely-used approximation in fluorescence microscopy. The scalar approximation models the propagation of light using a scalar-valued field U instead of the more realistic vector-valued electric field $\mathbf{E}$. Although the scalar model yields realistic results in many cases, the scalar field ignores polarization-dependent effects. The absorption and emission response of dipoles strongly depends on the polarization of the fields, so we need to use an electromagnetic model of light propagation to accurately model a microscope imaging dipoles.

This work lies at the intersection of three classes of fluorescence microscopy: (1) single molecule localization microscopy (SMLM), (2) spatial ensemble fluorescence microscopy including widefield, confocal, and light-sheet techniques, and (3) polarized fluorescence microscopy. We briefly review these three classes and focus on their use of the monopole and scalar approximations.

The SMLM community has pioneered the use of rigorous electromagnetic models of fluorescence microscopes [1, 2] [cite Novotny]. When a single molecule is fluorescing in the sample, the measured intensity pattern is strongly dependent on the orientation of the emitting molecule. Backlund [cite] and Lew [cite] [3] have shown that ignoring the orientation of fluorophores can bias position estimates, so the most accurate SMLM experiments must jointly estimate the position and orientation of each molecule.

Meanwhile, most fluorescence microscopists image ensembles of fluorophores and restore their images without considering the role that the monopole and scalar approximations play in the restoration process. A typical fluorescence microscopist is only interested in the spatial distribution of fluorophores, so they reason that they can ignore the orientation of the emitters.

A smaller community of microscopists is interested in measuring the orientation of ensembles of fluorophores [4] [Forkey, Goldman, Moerner, Oldenbourg]. These techniques typically use polarized illumination or polarized detection to make multiple measurements of the same object. Current angular restoration techniques use a model of the dipole excitation and emission processes [Fourkas] to recover the orientation of fluorophores using pixel-wise arithmetic, but these techniques do not perform any spatial restoration so they do not use all of the available information. To our knowledge no work has been done to model the complete spatio-angular response of fluorescence microscopes to ensembles of oriented fluorophores.

We begin in Section 2 by formulating the imaging problem mathematically. We start with an abstract description of fluorescence imaging systems and extend the usual monopole imaging model to dipoles. Along the way we introduce transfer functions that will allow us to efficiently analyze spatio-angular microscopes. In Section 3 we use the mathematical tools we developed in Section 2 to analyze and simulate a single-view paraxial epi-fluorescence microscope, and we demonstrate our model with four simple phantoms. Finally, in Section 4 we discuss the results and their broader implications.

2. Theory

We begin our analysis with the abstract Hilbert space formalism of Barrett and Myers [5]. Our first task is to formulate the imaging process as a mapping between two Hilbert spaces $\mathcal{H} : \mathbb{U} \to \mathbb{V}$, where $\mathbb{U}$ is a set than contains all possible objects, $\mathbb{V}$ is a set that contains all possible datasets, and $\mathcal{H}$ is a model of the instrument that maps between these two spaces. We denote (possibly infinite-dimensional) Hilbert-space vectors in $\mathbb{U}$ with $\mathbf{f}$, Hilbert-space vectors in $\mathbb{V}$ with $\mathbf{g}$, and the mapping between the spaces with

$$\mathbf{g} = \mathcal{H}\mathbf{f}. \tag{1}$$

Once we have identified the spaces $\mathbb{U}$ and $\mathbb{V}$, we can start expressing the mapping between the spaces in a specific object-space and data-space basis. In most cases the easiest mapping to find uses a delta-function basis—we expand object and data space into delta functions, then express the mapping as an integral transform. After finding this mapping we can start to investigate the same mapping in different bases.

The above discussion is quite abstract, but it is a powerful point of view that will enable us to draw new conclusions about all fluorescence microscopes. In Section 2.1 we will demonstrate the formalism by examining a familiar monopole imaging model, and we will demonstrate the mapping in between object and data in two different bases. In Section 2.2 we will extend the monopole imaging model to dipoles and examine the mapping in four different bases.

2.1. Monopole imaging in different bases

We start by considering a microscope that images a field of in-focus monopoles by recording the irradiance on a two-dimensional detector. This section treads familiar ground, but it serves to establish the concepts and notation that will be necessary when we extend to the dipole case.

We can represent the object as a function that assigns a real number to each point on a plane, so we identify object space as $\mathbb{U} = \mathbb{L}_2(\mathbb{R}^2)$. Similarly, we have a two-dimensional detector that measures a real number at every point on a plane, so data space is the same set $\mathbb{V} = \mathbb{L}_2(\mathbb{R}^2)$.

Next, we name the representations of our object and data in a specific basis. In a delta function basis the object can be represented by a function $f(\mathbf{r}_o)$ called the *monopole density*—the number of monopoles per unit area at the two-dimensional position $\mathbf{r}_o$. Similarly, in a delta function basis the data can be represented by a function $g'(\mathbf{r}'_d)$ called the *irradiance*—the power received by a surface per unit area at position $\mathbf{r}'_d$. It may seem pedantic to emphasize that these representations are in a delta function basis, but we highlight this point to make it clear that the delta function basis is not special—we can choose a different basis at will.

A reasonable starting point is to assume that the relationship between the object and the data is *linear*—this is usually true in fluorescence microscopes since fluorophores emit incoherently, so a scaled sum of fluorophores will result in a scaled sum of the irradiance patterns created by the individual fluorophores. If the mapping is linear, we can write the irradiance as a weighted integral over a field of monopoles

$$g'(\mathbf{r}'_d) = \int_{\mathbb{R}^2} d\mathbf{r}_o \, h'(\mathbf{r}'_d, \mathbf{r}_o) f(\mathbf{r}_o), \tag{2}$$

where $h'(\mathbf{r}_d', \mathbf{r}_o)$ is the irradiance at position $\mathbf{r}'_d$ created by a point source at $\mathbf{r}_o$.

The irradiance pattern measured by many fluorescence microscopes can be modeled (at least approximately) as a magnifier with shift-invariant blur

$$g'(\mathbf{r}'_d) = \int_{\mathbb{R}^2} d\mathbf{r}_o \, h'(\mathbf{r}'_d - m\mathbf{r}_o) f(\mathbf{r}_o), \tag{3}$$

where m is a magnification factor. To simplify our analysis we define a demagnified detector coordinate $\mathbf{r}_d = \mathbf{r}'_d/m$ and a normalization factor that corresponds to the total power incident on the detector plane due to a point source $P_{\mathrm{mono}} = \int_{\mathbb{R}^2} d\mathbf{r} \, h'(m\mathbf{r})$. We use these scaling factors to define the *point spread function* as

$$h(\mathbf{r}_d - \mathbf{r}_o) = \frac{h'(m[\mathbf{r}_d - \mathbf{r}_o])}{P_{\mathrm{mono}}}, \tag{4}$$

and the *scaled irradiance* as

$$g(\mathbf{r}_d) = \frac{g'(m\mathbf{r}_d)}{P_{\mathrm{mono}}}. \tag{5}$$

With these definitions we can express the mapping between the object and the data as a familiar convolution

$$g(\mathbf{r}_d) = \int_{\mathbb{R}^2} d\mathbf{r}_o \, h(\mathbf{r}_d - \mathbf{r}_o) f(\mathbf{r}_o), \tag{6}$$
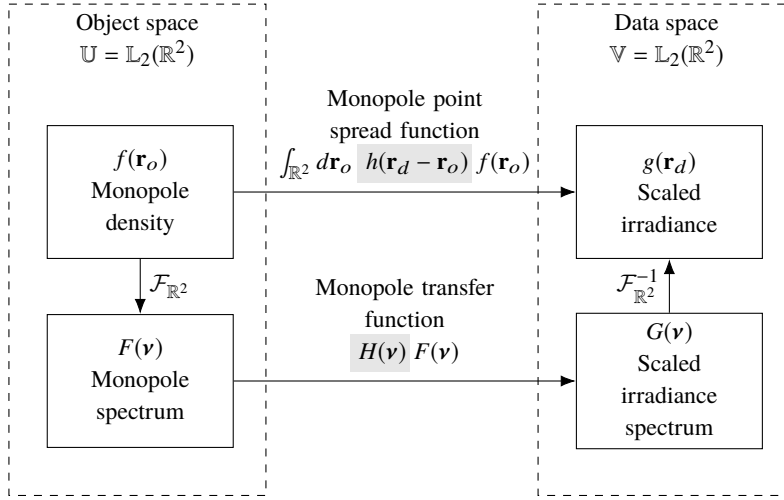
Fig. 1. The mapping between the object and data space of a monopole fluorescence microscope can be computed in two different bases—a delta function basis and a spatial harmonic basis. The change of basis is given by the two-dimensional Fourier transform denoted $\mathcal{F}_{\mathbb{R}^2}$.

which will allow us to analyze this class of microscopes without carrying magnification or normalization factors. We will mostly be using scaled coordinates, so we have adopted a slightly unusual convention of using primes to denote unscaled coordinates.

We have chosen to normalize the point spread function so that

$$\int_{\mathbb{R}^2} d\mathbf{r}\, h(\mathbf{r}) = 1. \tag{7}$$

The monopole point spread function corresponds to a measurable irradiance, so it is always real-valued and positive.

The mapping between the object and the data in linear shift-invariant microscopes takes a particularly simple form in a spatial harmonic basis. If we apply the Fourier convolution theorem to Eq. 6 we find that

$$G(\boldsymbol{\nu}) = H(\boldsymbol{\nu})F(\boldsymbol{\nu}), \tag{8}$$

where we define the *scaled irradiance spectrum* as

$$G(\boldsymbol{\nu}) = \int_{\mathbb{R}^2} d\mathbf{r}\, g(\mathbf{r}) \exp(-2\pi i \mathbf{r} \cdot \boldsymbol{\nu}), \tag{9}$$

the *monopole transfer function* as

$$H(\boldsymbol{\nu}) = \int_{\mathbb{R}^2} d\mathbf{r}\, h(\mathbf{r}) \exp(-2\pi i \mathbf{r} \cdot \boldsymbol{\nu}), \tag{10}$$

and the *monopole spectrum* as

$$F(\boldsymbol{\nu}) = \int_{\mathbb{R}^2} d\mathbf{r}\, f(\mathbf{r}) \exp(-2\pi i \mathbf{r} \cdot \boldsymbol{\nu}). \tag{11}$$

The monopole point spread function is normalized and real-valued, so we know that the monopole transfer function is normalized $H(0) = 1$ and conjugate-symmetric $H(-\boldsymbol{\nu}) = H^*(\boldsymbol{\nu})$.

Notice that Eqs. 6 and 8 are expressions of the same mapping between object and data space in different bases. Figure 1 summarizes the relationship between object and data space in both bases.

We have used the term *monopole transfer function* instead of the more common *optical transfer function*. We define the optical transfer function as the mapping between an input irradiance spectrum and an output irradiance spectrum in an optical system. With this definition the optical transfer function is not necessarily the same as the monopole transfer function. For example, consider a light sheet illumination scheme where a sheet of the sample is illuminated and an orthogonal detection arm collects the emitted fluorescence. Both the excitation path and the detection path can be described by optical transfer functions, and the monopole transfer function is given by the convolution of the two optical transfer functions. We will see that this is a valuable distinction when we consider dipole transfer functions.

2.1.1. Monopole coherent transfer functions

Although the Fourier transform can be used to calculate the monopole transfer function directly from the monopole point spread function, there is a well-known alternative that exploits coherent transfer functions. The key idea is that the monopole point spread function can always be written as the absolute square of a scalar-valued *monopole coherent spread function* defined as

$$h(\mathbf{r}) = |c(\mathbf{r})|^2.$$ (12)

Physically, the monopole coherent spread function is the scalar-valued field on the detector with appropriate scaling.

Since the monopole transfer function is given by the two-dimensional Fourier transform of the monopole point spread function

$$H(\boldsymbol{\nu}) = \int_{\mathbb{R}^2} d\mathbf{r}\, h(\mathbf{r}) \exp[-2\pi i \mathbf{r} \cdot \boldsymbol{\nu}],$$ (13)

we can plug in Eq. 12 and use the autocorrelation theorem to rewrite the monopole transfer function as

$$H(\boldsymbol{\nu}) = \int_{\mathbb{R}^2} d\boldsymbol{\tau}\, C(\boldsymbol{\tau}) C^*(\boldsymbol{\tau} - \boldsymbol{\nu}),$$ (14)

where z^* denotes the complex conjugate of z, and we have introduced the *monopole coherent transfer function* as the two-dimensional Fourier transform of the orientation-dependent coherent spread function

$$C(\boldsymbol{\tau}) = \int_{\mathbb{R}^2} d\mathbf{r}\, c(\mathbf{r}) \exp[-2\pi i \mathbf{r} \cdot \boldsymbol{\tau}].$$ (15)

Physically, the monopole coherent transfer function is the scalar-valued field in a Fourier plane of the detector (often called the pupil or aperture plane) with appropriate scaling. This provides a valuable shortcut for analyzing arbitrary microscopes since it is usually straightforward to calculate the field in the pupil. A typical approach for calculating the transfer functions is to (1) calculate the field in the pupil, (2) scale the field to find the coherent monopole transfer function, then (3) use the relationships in Figure 2 to calculate the other transfer functions.

2.2. Dipole imaging in different bases

Now we consider a microscope imaging a field of in-focus dipoles by recording the irradiance on a two-dimensional detector. A function that assigns a real number to each point on a plane is not sufficient to specify a field of dipoles because the dipoles can have different orientations.

$$|c(\mathbf{r})|^2$$

```
┌─────────────────────┐          ┌─────────────────────┐
│       c(r)          │   |c(r)|²│       h(r)           │
│  Coherent monpole   │─────────▶│  Monopole point      │
│  spread function    │          │  spread function     │
└─────────────────────┘          └─────────────────────┘
         │ F_R²                           │ F_R²
         ▼                                ▼
┌─────────────────────┐          ┌─────────────────────┐
│       C(τ)          │          │       H(ν)           │
│  Coherent monopole  │─────────▶│     Monopole         │
│  transfer function  │          │  transfer function   │
└─────────────────────┘          └─────────────────────┘
```

$$\int_{\mathbb{R}^2} d\boldsymbol{\tau}\, C(\boldsymbol{\tau}) C^*(\boldsymbol{\tau} - \boldsymbol{\nu})$$
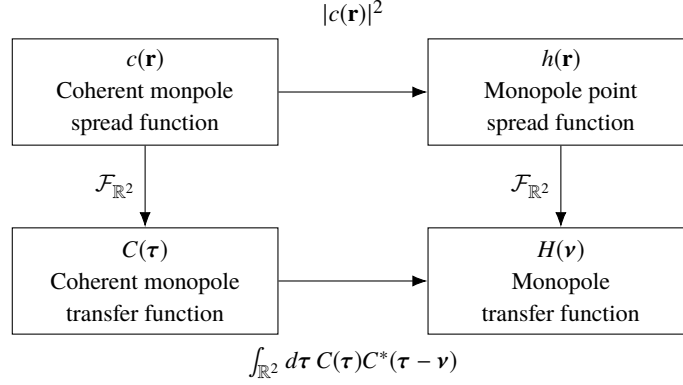
Fig. 2. The incoherent monopole transfer functions are related by a two-dimensional Fourier transform (right column). The coherent monopole transfer functions (left column) can be used to simplify the calculation of the remaining transfer functions.

To represent the object we need to extend object space to $\mathbb{U} = \mathbb{L}_2(\mathbb{R}^2 \times \mathbb{S}^2)$ where $\mathbb{S}^2$ is the two-dimensional sphere (the usual sphere embedded in $\mathbb{R}^3$).

In a delta function basis the object can be represented by a function $f(\mathbf{r}_o, \hat{\mathbf{s}}_o)$ called the *dipole density*—the number of dipoles at position $\mathbf{r}_o$ per unit area oriented along $\hat{\mathbf{s}}_o$ per unit solid angle. Similar to the monopole case, we model the mapping between the object and the irradiance in a delta function basis as an integral transform

$$g'(\mathbf{r}_d') = \int_{\mathbb{S}^2} d\hat{\mathbf{s}}_o \int_{\mathbb{R}^2} d\mathbf{r}_o\, h'(\mathbf{r}_d', \mathbf{r}_o, \hat{\mathbf{s}}_o) f(\mathbf{r}_o, \hat{\mathbf{s}}_o). \tag{16}$$

where $h'(\mathbf{r}_d', \mathbf{r}_o, \hat{\mathbf{s}}_o)$ is the irradiance at position $\mathbf{r}_d'$ created by a point source at $\mathbf{r}_o$ with orientation $\hat{\mathbf{s}}_o$. Once again, many fluorescence microscopes can be modeled as magnifiers with shift-invariant blur

$$g'(\mathbf{r}_d') = \int_{\mathbb{S}^2} d\hat{\mathbf{s}}_o \int_{\mathbb{R}^2} d\mathbf{r}_o\, h'(\mathbf{r}_d' - m\mathbf{r}_o, \hat{\mathbf{s}}_o) f(\mathbf{r}_o, \hat{\mathbf{s}}_o). \tag{17}$$

We define the same demagnified detector coordinate $\mathbf{r}_d = \mathbf{r}_d'/m$ and a new normalization factor that corresponds to the total power incident on the detector due to a spatial point source with an angularly uniform distribution of dipoles $P_{\text{dip}} = \int_{\mathbb{S}^2} d\hat{\mathbf{s}} \int_{\mathbb{R}^2} d\mathbf{r}\, h'(m\mathbf{r}, \hat{\mathbf{s}})$. We use these scaling factors to define the *dipole point spread function* as

$$h(\mathbf{r}_d - \mathbf{r}_o, \hat{\mathbf{s}}_o) = \frac{h'(m[\mathbf{r}_d - \mathbf{r}_o], \hat{\mathbf{s}}_o)}{P_{\text{dip}}}, \tag{18}$$

and the *scaled irradiance* as

$$g(\mathbf{r}_d) = \frac{g'(m\mathbf{r}_d)}{P_{\text{dip}}}. \tag{19}$$

With these definitions we can express the mapping between the object and the data as

$$g(\mathbf{r}_d) = \int_{\mathbb{S}^2} d\hat{\mathbf{s}}_o \int_{\mathbb{R}^2} d\mathbf{r}_o\, h(\mathbf{r}_d - \mathbf{r}_o, \hat{\mathbf{s}}_o) f(\mathbf{r}_o, \hat{\mathbf{s}}_o). \tag{20}$$

Similar to the monopole case, we have chosen to normalize the dipole point spread function so that

$$\int_{\mathbb{S}^2} d\hat{\mathbf{s}} \int_{\mathbb{R}^2} d\mathbf{r}\, h(\mathbf{r}, \hat{\mathbf{s}}) = 1. \tag{21}$$
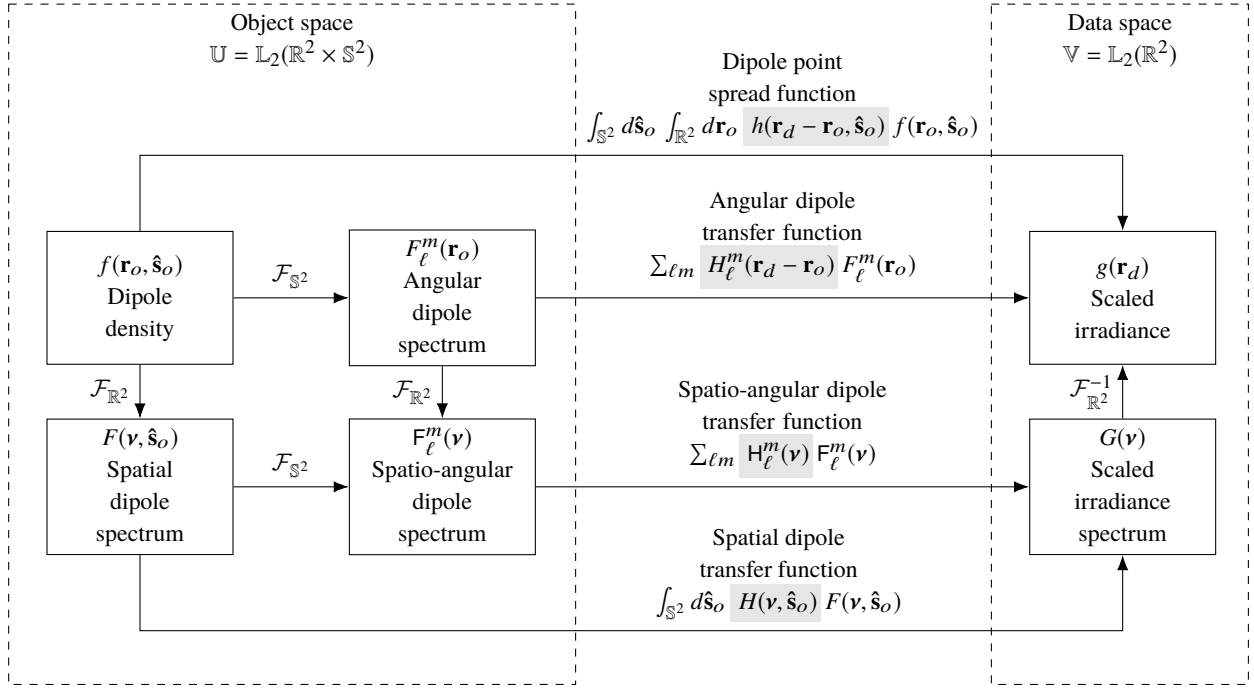
Fig. 3. The mapping between the object and data space of a dipole fluorescence microscope can be computed in four different bases—a delta function basis, a spatial-harmonic/angular-delta basis, a spatial-delta/spherical-harmonic basis, and a spatio-angular harmonic basis. The changes of basis are given by the two-dimensional Fourier transform denoted $\mathcal{F}_{\mathbb{R}^2}$ and the spherical Fourier transform denoted $\mathcal{F}_{\mathbb{S}^2}$.

The dipole point spread function is a measurable quantity, so it is real-valued and positive.

2.2.1. Spatial dipole transfer function

We can make our first change of basis by applying the Fourier-convolution theorem to Eq. 20 which yields

$$G(\nu) = \int_{\mathbb{S}^2} d\hat{s}\, H(\nu, \hat{s}) F(\nu, \hat{s}), \tag{22}$$

where we define the *spatial dipole transfer function* as

$$H(\nu, \hat{s}) = \int_{\mathbb{R}^2} d\mathbf{r}\, h(\mathbf{r}, \hat{s}) \exp(-2\pi i \mathbf{r} \cdot \nu), \tag{23}$$

and the *spatial dipole spectrum* as

$$F(\nu, \hat{s}) = \int_{\mathbb{R}^2} d\mathbf{r}\, f(\mathbf{r}, \hat{s}) \exp(-2\pi i \mathbf{r} \cdot \nu). \tag{24}$$

Since the dipole point spread function is normalized and real, we know that the spatial dipole transfer function is normalized $\int_{\mathbb{S}^2} d\hat{s}\, H(0, \hat{s}) = 1$ and conjugate-symmetric $H(-\nu, \hat{s}) = H^*(\nu, \hat{s})$.

This choice of basis is well suited for simulating and analyzing objects that are angularly sparse and spatially dense.

2.2.2. Angular dipole transfer function

The spherical harmonics are another set of convenient basis functions. We can change basis from spherical delta functions to spherical harmonics by applying the generalized Plancharel theorem for spherical functions

$$\int_{\mathbb{S}^2} d\hat{\mathbf{s}}\, p(\hat{\mathbf{s}})q(\hat{\mathbf{s}}) = \sum_{\ell=0}^{\infty} \sum_{m=-\ell}^{\ell} P_\ell^m Q_\ell^m, \tag{25}$$

where $p(\hat{\mathbf{s}})$ and $q(\hat{\mathbf{s}})$ are arbitrary functions on the sphere, P_ℓ^m and Q_ℓ^m are their spherical Fourier transforms defined by

$$P_\ell^m = \int_{\mathbb{S}^2} d\hat{\mathbf{s}}\, p(\hat{\mathbf{s}})Y_\ell^{m*}(\hat{\mathbf{s}}), \tag{26}$$

and $Y_\ell^m(\hat{\mathbf{s}})$ are the spherical harmonic functions defined in Appendix B. Eq. 25 expresses the fact that scalar products are invariant under a change of basis (see Eq. 3.78 of [5]). The left-hand side of Eq. 25 is the scalar product of $\mathbb{L}_2(\mathbb{S}^2)$ functions in a delta function basis and the right hand side is the scalar product of $\mathbb{L}_2(\mathbb{S}^2)$ functions in a spherical harmonic function basis. Applying Eq. 25 to Eq. 20 yields

$$g(\mathbf{r}_d) = \sum_{\ell=0}^{\infty} \sum_{m=-\ell}^{\ell} H_\ell^m(\mathbf{r}_d - \mathbf{r}_o)F_\ell^m(\mathbf{r}_o) \tag{27}$$

where we have defined the *angular dipole transfer function* as

$$H_\ell^m(\mathbf{r}) = \int_{\mathbb{S}^2} d\hat{\mathbf{s}}\, h(\mathbf{r}, \hat{\mathbf{s}})Y_\ell^{m*}(\hat{\mathbf{s}}), \tag{28}$$

and the *angular dipole spectrum* as

$$F_\ell^m(\mathbf{r}) = \int_{\mathbb{S}^2} d\hat{\mathbf{s}}\, f(\mathbf{r}, \hat{\mathbf{s}})Y_\ell^{m*}(\hat{\mathbf{s}}). \tag{29}$$

Since the dipole point spread function is normalized and real-valued, we know that the angular dipole transfer function is normalized $\int_{\mathbb{R}^2} d\mathbf{r}\, H_0^0(\mathbf{r}) = 1$ and conjugate symmetric $H_\ell^{-m}(\mathbf{r}) = (-1)^m H_\ell^{m*}(\mathbf{r})$.

This basis is well suited for simulating and analyzing objects that are spatially sparse and angularly dense.

2.2.3. Spatio-angular dipole transfer function

We can arrive at our final basis in two ways: by applying the generalized Plancharel theorem for spherical functions to Eq. 22 or by applying the Fourier convolution theorem to Eq. 27. We follow the second path and find that

$$G(\boldsymbol{\nu}) = \sum_{\ell=0}^{\infty} \sum_{m=-\ell}^{\ell} \mathsf{H}_\ell^m(\boldsymbol{\nu})\mathsf{F}_\ell^m(\boldsymbol{\nu}), \tag{30}$$

where we have defined the *spatio-angular dipole transfer function* as

$$\mathsf{H}_\ell^m(\boldsymbol{\nu}) = \int_{\mathbb{S}^2} d\hat{\mathbf{s}}\, H(\boldsymbol{\nu}, \hat{\mathbf{s}})Y_\ell^{m*}(\hat{\mathbf{s}}), \tag{31}$$

and the *spatio-angular dipole spectrum* as

$$\mathsf{F}_\ell^m(\boldsymbol{\nu}) = \int_{\mathbb{S}^2} d\hat{\mathbf{s}}\, F(\boldsymbol{\nu}, \hat{\mathbf{s}}) Y_\ell^{m*}(\hat{\mathbf{s}}). \tag{32}$$

Since the dipole point spread function is normalized and real-valued, we know that the spatio-angular dipole transfer function is normalized $\mathsf{H}_0^0(0) = 1$ and conjugate symmetric $\mathsf{H}_\ell^{-m}(-\boldsymbol{\nu}) = (-1)^m \mathsf{H}_\ell^{m*}(\boldsymbol{\nu})$.

This basis is well suited for simulating and analyzing arbitrary samples because it exploits the sparsity of the imaging system. We will see this advantage explicitly in Section XXX when we calculate a specific spatio-angular dipole transfer function and see that it has an angular band limit.

Figure 3 summarizes the relationship between the four bases that we can use to compute the image of a field of dipoles. We reiterate that all four bases may be useful depending on the sparsity of the sample.

2.2.4. Dipole coherent transfer functions

Similar to the monopole case, there is efficient way to calculate the transfer functions using coherent transfer functions. The dipole point spread function can always be written as the absolute square of a vector-valued function called the *dipole coherent spread function*

$$h(\mathbf{r}, \hat{\mathbf{s}}) = |\mathbf{c}(\mathbf{r}, \hat{\mathbf{s}})|^2. \tag{33}$$

Physically, the dipole coherent spread function is an appropriately scaled vector-valued electric field on the detector. We need a vector-valued coherent transfer function since the polarization of the field plays a significant role in dipole imaging.

Since the spatial dipole transfer function is given by the two-dimensional Fourier transform of the dipole point spread function

$$H(\boldsymbol{\nu}) = \int_{\mathbb{R}^2} d\mathbf{r}\, h(\mathbf{r}, \hat{\mathbf{s}}) \exp[-2\pi i \mathbf{r} \cdot \boldsymbol{\nu}], \tag{34}$$

we can plug in Eq. 33 and use the autocorrelation theorem to rewrite the spatial dipole transfer function as

$$H(\boldsymbol{\nu}) = \int_{\mathbb{R}^2} d\boldsymbol{\tau}\, \mathbf{C}(\boldsymbol{\tau}, \hat{\mathbf{s}}) \mathbf{C}^\dagger(\boldsymbol{\tau} - \boldsymbol{\nu}, \hat{\mathbf{s}}), \tag{35}$$

where we have introduced the *dipole coherent transfer function* $\mathbf{C}(\boldsymbol{\tau}, \hat{\mathbf{s}})$ as the two-dimensional Fourier transform of the dipole coherent spread function

$$\mathbf{C}(\boldsymbol{\tau}, \hat{\mathbf{s}}) = \int_{\mathbb{R}^2} d\mathbf{r}\, \mathbf{c}(\mathbf{r}, \hat{\mathbf{s}}) \exp[-2\pi i \mathbf{r} \cdot \boldsymbol{\tau}]. \tag{36}$$

Physically, the dipole coherent transfer function corresponds to the vector-valued electric field created by a dipole with oriented along $\hat{\mathbf{s}}$ in a Fourier plane of the detector with appropriate scaling. As with the monopole case we can calculate the dipole-orientation-dependent fields in the pupil plane, scale them appropriately to find the dipole coherent transfer function, the use the relationships in Figure 4 to calculate the other transfer functions. Note that we could define coherent equivalents for all four incoherent transfer functions, but we restrict ourselves to these two since they are the most useful for our calculations.
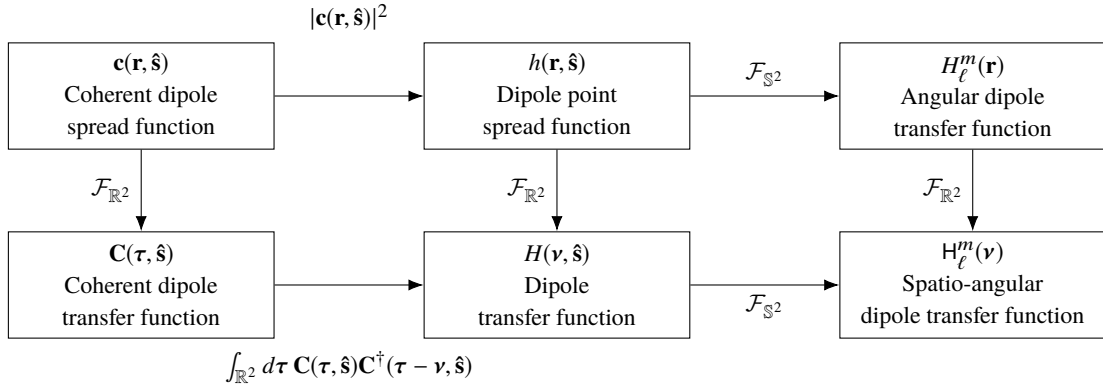
$|\mathbf{c}(\mathbf{r}, \hat{\mathbf{s}})|^2$

| $\mathbf{c}(\mathbf{r}, \hat{\mathbf{s}})$ Coherent dipole spread function | → | $h(\mathbf{r}, \hat{\mathbf{s}})$ Dipole point spread function | $\xrightarrow{\mathcal{F}_{\mathbb{S}^2}}$ | $H_\ell^m(\mathbf{r})$ Angular dipole transfer function |

$\mathcal{F}_{\mathbb{R}^2}$ $\mathcal{F}_{\mathbb{R}^2}$ $\mathcal{F}_{\mathbb{R}^2}$

| $\mathbf{C}(\boldsymbol{\tau}, \hat{\mathbf{s}})$ Coherent dipole transfer function | → | $H(\boldsymbol{\nu}, \hat{\mathbf{s}})$ Dipole transfer function | $\xrightarrow{\mathcal{F}_{\mathbb{S}^2}}$ | $\mathsf{H}_\ell^m(\boldsymbol{\nu})$ Spatio-angular dipole transfer function |

$\int_{\mathbb{R}^2} d\boldsymbol{\tau} \, \mathbf{C}(\boldsymbol{\tau}, \hat{\mathbf{s}})\mathbf{C}^\dagger(\boldsymbol{\tau} - \boldsymbol{\nu}, \hat{\mathbf{s}})$

Fig. 4. There is one incoherent transfer function for each set of object-space basis functions, and these transfer functions are related by two-dimensional and spherical Fourier transforms— see center and right columns. There are an additional pair of coherent transfer functions that are useful for calculating the incoherent transfer functions—see left column.

3. Results

In this section we apply the tools we developed in the previous sections to analyze a paraxial epi-fluorescence microscope. We start by reviewing the derivation of the monopole point spread function in preparation for the derivation of the orientation-dependent point spread function. We conclude the section by analyzing the dipole imaging map in the four bases we described earlier.

TODO: Define and discuss paraxial. 4f, illumination uniformity and ignoring in monopole Where are excitation and detection dipoles parallel.

3.1. Monopole point spread function of a paraxial epi-fluorescence microscope

In this section we derive the form of the monopole point spread function $h(\mathbf{r}_d - \mathbf{r}_o)$. First, we place a monopole emitter at the focal point of an objective lens and calculate the field $U_{\text{bfp}}(\mathbf{r}_b)$ created in the back focal plane. We can model a paraxial thin lens as a quadratic phase element, so it converts an incident spherical wave to a plane wave in the back focal plane with a sharp cutoff at the exit pupil of the lens

$$U_{\text{bfp}}(\mathbf{r}_b) \propto \Pi\left(\frac{|\mathbf{r}_b|}{2\alpha}\right) \equiv \begin{cases} 1 & \text{if} \quad |\mathbf{r}_b| < \alpha, \\ 0 & \text{else,} \end{cases} \tag{37}$$

where $\mathbf{r}_b$ is the two-dimensional coordinate in the back focal plane and α is the collection half angle—see Figure XXX.

A central result of Fourier optics is that the fields one focal distance from either side of a paraxial lens are related by a scaled two-dimensional Fourier transform. If we place a detector in the focal plane of the tube lens, then the field on the detector $U_{\text{det}}(\mathbf{r}_d)$ is given by

$$U_{\text{det}}(\mathbf{r}_d) \propto \frac{J_1(k\alpha|\mathbf{r}_d|)}{|\mathbf{r}_d|}. \tag{38}$$

where $J_n(x)$ denotes the Bessel function of the first kind of order n, and $k = 2\pi/\lambda$ is the wave number.

Finally, the detector measures the irradiance instead of the field, so we take the modulus squared of the field to find that the measurable irradiance created by a single monopole radiator

at the origin is the familiar Airy disk

$$h(\mathbf{r}_d, \mathbf{r}_o = 0) \propto |U_{\text{det}}(\mathbf{r}_d)|^2 = \left[\frac{J_1(k\alpha|\mathbf{r}_d|)}{|\mathbf{r}_d|} \right]^2. \tag{39}$$

Shifting the monopole in the transverse plane will introduce a linear phase factor in the back focal plane which will manifest as a shift on the detector due to the Fourier shift theorem. Therefore, the monopole imaging system is shift invariant and we can rewrite the irradiance on the detector due to a monopole at $\mathbf{r}_o$ as

$$h(\mathbf{r}_d, \mathbf{r}_o) = h(\mathbf{r}_d - \mathbf{r}_o). \tag{40}$$

We have modeled a microscope with unit magnification, but a similar point spread function can be found for magnifying microscopes by making a change of variables (see [5], section 7.2.7).

Rotating a monopole will leave its image unchanged. Therefore, our imaging system is rotation invariant and we can simplify the orientation-dependent point spread function further with

$$h(\mathbf{r}_d - \mathbf{r}_o) = h(|\mathbf{r}_d - \mathbf{r}_o|). \tag{41}$$

3.2. Orientation-dependent point spread function of a paraxial epi-fluorescence microscope

In this section we will calculate the orientation-dependent point spread function $h(\mathbf{r}_d - \mathbf{r}_o, \hat{\mathbf{s}})$ of a paraxial epi-fluorescence microscope. We can make our first simplifying step by realizing the excitation and detection processes are incoherent, which means that the orientation-dependent PSF is separable:

$$h(\mathbf{r}_d, \mathbf{r}_o, \hat{\mathbf{s}}_o) = h_{\text{exc}}(\mathbf{r}_o, \hat{\mathbf{s}}_o) \, h_{\text{det}}(\mathbf{r}_d, \mathbf{r}_o, \hat{\mathbf{s}}_o). \tag{42}$$

We can calculate the excitation and detection terms separately then take their product to find the complete orientation-dependent point spread function.

3.2.1. Orientation-dependent excitation model

When we developed the monopole imaging model we ignored the excitation process because we excited the fluorophores with a spatially uniform excitation beam and monopoles have no orientation dependence. For the dipole imaging model we must model the excitation process because the excitation process is rarely angularly uniform (carefully calibrated TIRF systems are an exception).

In this section we will calculate the excitation kernel $h_{\text{exc}}(\mathbf{r}_o, \hat{\mathbf{s}}_o)$ for the paraxial epi-illumination microscope under unpolarized (TODO: Define/cite) Köehler illumination shown in Figure 5. We will only consider spatially uniform excitation, so the excitation kernel will not depend on $\mathbf{r}_o$

$$h_{\text{exc}}(\mathbf{r}_o, \hat{\mathbf{s}}_o) = h_{\text{exc}}(\hat{\mathbf{s}}_o). \tag{43}$$

We can interpret $h_{\text{exc}}(\hat{\mathbf{s}}_o)$ as the relative probability of exciting a molecule with dipole orientation $\hat{\mathbf{s}}_o$. Our approach is similar to previous work [6, 7], but here we consider paraxial, incoherent, and unpolarized illumination (TODO improve).

We start by expressing the dipole moment $\hat{\mathbf{s}}_o$ in Cartesian coordinates

$$\hat{\mathbf{s}}_o = s_x \hat{\mathbf{x}} + s_y \hat{\mathbf{y}} + s_z \hat{\mathbf{z}}. \tag{44}$$

We place the dipole in the focal plane of an aplanatic and polarization-preserving objective lens with its optical axis aligned with the $\hat{\mathbf{z}}$ axis. Next, we place a spatially incoherent, spatially
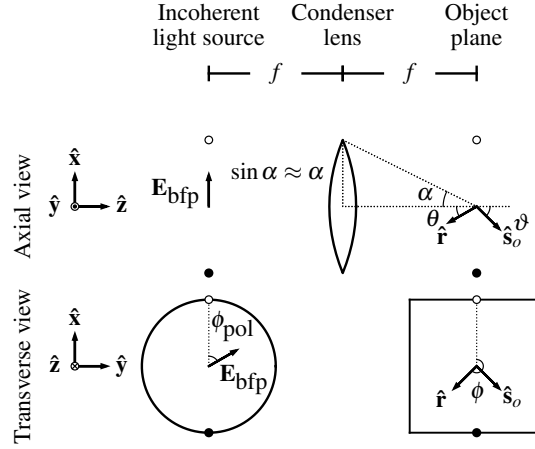
Fig. 5. Illumination geometry and coordinates for a paraxial epifluorescence microscope. An unpolarized and incoherent light source (or its image) is in the back focal plane of the condenser lens.

uniform, unpolarized light source (or its image) in the back aperture of the objective lens to illuminate the focal plane. In this geometry each point in the back focal plane generates a plane wave that illuminates the sample.

To model the unpolarized light source we will use polarized ray tracing [8] to find the response for a single polarized ray, then integrate over the rays and all polarizations to find the complete response. First, we model the electric field at every point on the back focal plane as

$$\mathbf{E}_{\text{bfp}}(\phi_{\text{pol}}) \propto \cos \phi_{\text{pol}} \hat{\mathbf{x}} + \sin \phi_{\text{pol}} \hat{\mathbf{y}}, \tag{45}$$

where ϕ_{pol} is the polarization orientation and $\{\hat{\mathbf{x}}, \hat{\mathbf{y}}\}$ are transverse Cartesian basis vectors. Note that Eq. 45 describes the incoherent electric fields at every point in the back focal plane— it does not describe a coherent plane wave. To find the electric field immediately after the paraxial lens we apply a position-dependent rotation matrix (see the rotation matrices in [1, 8] under the paraxial approximation):

$$\mathbf{E}_{\text{ff}}(\theta, \phi, \phi_{\text{pol}}) \propto \begin{bmatrix} 1 & 0 & \theta \cos \phi \\ 0 & 1 & \theta \sin \phi \\ -\theta \cos \phi & -\theta \sin(\phi) & 1 \end{bmatrix} \begin{bmatrix} \cos \phi_{\text{pol}} \\ \sin \phi_{\text{pol}} \\ 0 \end{bmatrix}, \tag{46}$$

so that

$$\mathbf{E}_{\text{ff}}(\theta, \phi, \phi_{\text{pol}}) \propto \cos \phi_{\text{pol}} \hat{\mathbf{x}} + \sin \phi_{\text{pol}} \hat{\mathbf{y}} - \theta \cos(\phi - \phi_{\text{pol}}) \hat{\mathbf{z}}. \tag{47}$$

The probability that a dipole oriented along $\hat{\mathbf{s}}_o$ is excited by a ray with electric field $\mathbf{E}$ is given by

$$|\mathbf{E}_{\text{ff}}(\theta, \phi, \phi_{\text{pol}}) \cdot \hat{\mathbf{s}}_o|^2 \propto s_x^2 \cos^2 \phi_{\text{pol}} + s_y^2 \sin^2 \phi_{\text{pol}} + s_z^2 \theta^2 \cos^2(\phi - \phi_{\text{pol}}). \tag{48}$$

To find the complete excitation kernel we need to integrate Eq. 48 over all polarization orientations and rays:

$$h_{\text{exc}}(\hat{\mathbf{s}}_o) \propto \int_0^\alpha \theta d\theta \int_0^{2\pi} d\phi \int_0^{2\pi} d\phi_{\text{pol}} |\mathbf{E}_{\text{ff}}(\theta, \phi, \phi_{\text{pol}}) \cdot \hat{\mathbf{s}}_o|^2. \tag{49}$$

Plugging Eq. 48 into Eq. 49, evaluating the integrals, and dropping constants gives

$$h_{\text{exc}}(\vartheta) \propto s_x^2 + s_y^2 + \frac{1}{2}\alpha^2 s_z^2. \tag{50}$$

We can rewrite the excitation kernel in terms of a single variable with the substitutions $s_x^2 + s_y^2 = \sin^2 \vartheta$ and $s_z^2 = \cos^2 \vartheta$:

$$h_{\text{exc}}(\vartheta) \propto \sin^2 \vartheta + \frac{1}{2}\alpha^2 \cos^2 \vartheta. \tag{51}$$

Figure 6 shows the excitation response as a function of inclination angle ϑ and excitation half angle α. The largest variation of the excitation kernel occurs when the maximum excitation angle is zero—plane-wave illumination. As α grows, dipoles parallel to the optic axis are more likely to be excited and the variation of the excitation kernel decreases.
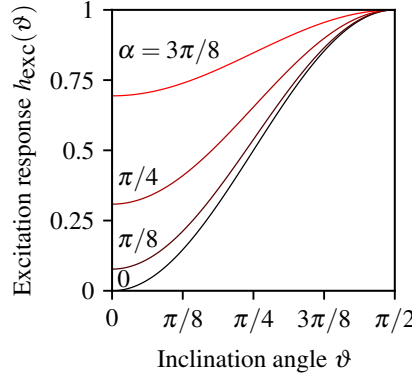
Fig. 6. Dipole excitation kernel $h_{\text{exc}}(\vartheta)$ as a function of inclination angle ϑ and excitation half angle α.

3.2.2. Orientation-dependent dipole detection model

In this section we will calculate the detection kernel of an epi-detection microscope—the irradiance on the detector due to a single dipole with fixed position and orientation. [TODO Improve] Our approach mimics existing work [1, 9, 10], but we restrict ourselves to the paraxial approximation.

We consider a single dipole emitter at the origin with a fixed dipole emission moment oriented along $\hat{\mathbf{s}}_o$. The electric field at a position $\mathbf{r}$ far from the dipole is given by

$$\mathbf{E}_{\text{ff}}(\mathbf{r}, \hat{\mathbf{s}}_o) \propto \frac{\exp[ik|\hat{\mathbf{r}}|]}{|\hat{\mathbf{r}}|} \hat{\mathbf{r}} \times \hat{\mathbf{s}}_o \times \hat{\mathbf{r}}. \tag{52}$$

We place the dipole in the focal plane of the same $4f$ imaging system we considered in the monopole case—see Figure 7. The dipole emits spherical wavefronts so we can reuse our argument for shift invariance and drop the phase dependence of the electric field

$$\mathbf{E}_{\text{ff}}(\mathbf{r}, \hat{\mathbf{s}}_o) \propto \hat{\mathbf{r}} \times \hat{\mathbf{s}}_o \times \hat{\mathbf{r}} \tag{53}$$

We also note that we can rewrite a shift-invariant kernel as

$$h_{\text{det}}(\mathbf{r}_d, \mathbf{r}_o, \hat{\mathbf{s}}_o) = h_{\text{det}}(\mathbf{r}_d - \mathbf{r}_o, \hat{\mathbf{s}}_o), \tag{54}$$
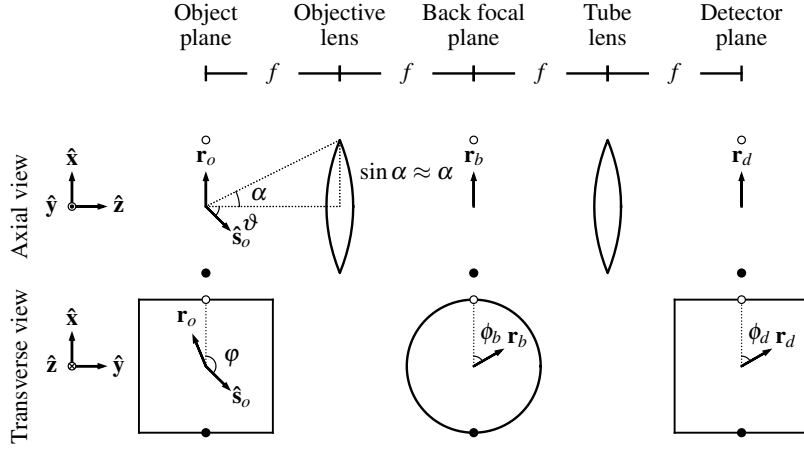
Fig. 7. Detection geometry and coordinates. We calculate the detection kernel $h_{\text{det}}(\mathbf{r}_d, \mathbf{r}_o, \hat{\mathbf{s}}_o)$ for a paraxial $4f$ imaging system.

which will simplify our derivation—we only need to calculate the response for a dipole positioned along the optic axis. We can rewrite the cross products in terms of a matrix multiplication

$$\mathbf{E}_{\text{ff}}(\mathbf{r}, \hat{\mathbf{s}}_o) \propto [\overset{\leftrightarrow}{\mathbf{I}} - \hat{\mathbf{r}}\hat{\mathbf{r}}^{\dagger}]\hat{\mathbf{s}}_o, \tag{55}$$

where $\overset{\leftrightarrow}{\mathbf{I}}$ is a 3×3 identity matrix. If we place the molecule in the focal plane of an aplanatic and polarization-preserving objective lens with the lens' optical axis aligned with the $\hat{\mathbf{z}}$ axis, then we can find the electric field in the back focal plane by multiplying the electric field with a position-dependent rotation matrix and truncating waves outside the detection collection half angle α

$$\mathbf{E}_{\text{bfp}}(\mathbf{r}, \hat{\mathbf{s}}_o) \propto \mathbf{R}_{\text{obj}}(\hat{\mathbf{r}})[\overset{\leftrightarrow}{\mathbf{I}} - \hat{\mathbf{r}}\hat{\mathbf{r}}^{\dagger}]\hat{\mathbf{s}}_o \Pi\left(\frac{\theta}{2\alpha}\right). \tag{56}$$

After plugging in paraxial positions

$$\hat{\mathbf{r}}(\theta, \phi) \approx \theta \cos\phi \hat{\mathbf{x}} + \theta \sin\phi \hat{\mathbf{y}} + \hat{\mathbf{z}}, \tag{57}$$

and the paraxial rotation matrix

$$\mathbf{R}_{\text{obj}}(\theta, \phi) = \begin{bmatrix} 1 & 0 & -\theta \cos\phi \\ 0 & 1 & -\theta \sin\phi \\ -\theta \cos\phi & -\theta \sin(\phi) & 1 \end{bmatrix}, \tag{58}$$

then dropping the θ^2 $\hat{\mathbf{z}}$ components and changing from spherical coordinates to cylindrical coordinates by substituting (r_b, ϕ_b) for (θ, ϕ) we find that

$$\mathbf{E}_{\text{bfp}}(r_b, \phi_b, \hat{\mathbf{s}}_o) \propto \left\{ [s_x - s_z r_b \cos\phi_b]\hat{\mathbf{x}} + [s_y - s_z r_b \sin\phi_b]\hat{\mathbf{y}} \right\} \Pi\left(\frac{r_b}{2\alpha}\right). \tag{59}$$

Equation 59 is easier to work with if we introduce the radial vector field $\hat{\boldsymbol{\rho}} = \cos\phi_b \hat{\mathbf{x}} + \sin\phi_b \hat{\mathbf{y}}$ and rewrite as

$$\mathbf{E}_{\text{bfp}}(r_b, \phi_b, \hat{\mathbf{s}}_o) \propto \left\{ s_x \hat{\mathbf{x}} + s_y \hat{\mathbf{y}} - s_z r_b \hat{\boldsymbol{\rho}} \right\} \Pi\left(\frac{r_b}{2\alpha}\right). \tag{60}$$

Equation 60 shows that the transverse components of the dipole (s_x, s_y) create linear vector fields in the back focal plane $(\hat{\mathbf{x}}, \hat{\mathbf{y}})$ while the axial component of the dipole s_z creates a radial vector field in the back focal plane $\hat{\mathbf{z}}$.

We complete the $4f$ system by placing a tube lens one focal length from the back focal plane and a planar detector—see Figure 7. Under the paraxial approximation we can find the electric field in the detector plane by taking the Fourier transform of the field in the back focal plane [11]

$$\mathbf{E}_{\text{det}}(\mathbf{r}_d, \hat{\mathbf{s}}_o) = \int_{\mathbb{R}^2} d\mathbf{r}_b \mathbf{E}_{\text{bfp}}(\mathbf{r}_b) \exp\left[ik\, \mathbf{r}_b \cdot \mathbf{r}_d\right]. \tag{61}$$

We evaluate the integral in Appendix A and show that

$$\mathbf{E}_{\text{det}}(r_d, \hat{\mathbf{s}}_o) \propto \frac{J_1(k\alpha r_d)}{r_d} s_x \hat{\mathbf{x}} + \frac{J_1(k\alpha r_d)}{r_d} s_y \hat{\mathbf{y}} - i\alpha \frac{J_2(k\alpha r_d)}{r_d} s_z \hat{\boldsymbol{\rho}}. \tag{62}$$

Once again we find that the transverse component of the dipole creates a linear field and the axial component of the dipole creates a radial field, but on the detector the linear and radial fields are out of phase by $\pi/2$. This crucial phase factor is a direct consequence of the fact that the linear fields are real and even—the Fourier transform of a real and even function is real and even—and the radial fields are real and odd—the Fourier transform of a real and odd function is imaginary and odd.

Our final step is to calculate the irradiance on the detector

$$h_{\text{det}}(r_d, \hat{\mathbf{s}}_o) \propto |\mathbf{E}_{\text{det}}(r_d, \hat{\mathbf{s}}_o)|^2. \tag{63}$$

The irradiance is the sum of the contributions from the linear and radial fields since their fields are out of phase, so

$$h_{\text{det}}(r_d, \vartheta) \propto a_1(r_d) \sin^2 \vartheta + \frac{1}{2}\alpha^2 a_2(r_d) \cos^2 \vartheta, \tag{64}$$

where we have defined

$$a_n(r_d) \equiv \frac{n}{\pi} \left[\frac{J_n(k\alpha r_d)}{r_d} \right]^2. \tag{65}$$

Notice that we retain the α^2 irradiance term even though we dropped θ^2 electric field terms since these terms would become θ^4 irradiance terms.

Figures 8 and 9 summarize the most important features of the dipole detection model. When α is very small the detection kernel is the usual Airy pattern weighted by $\sin^2 \vartheta$. Note that the monopole detection model ignores the $\sin^2 \vartheta$ dependence—see Figure 9 a) and b). As α grows, the relative contribution of the higher-order Airy pattern increases. The most important result is that the dipole detection model is not separable into the product of a spatial and angular kernel—even under the paraxial approximation. The detection model is only separable when α approaches zero, which is almost never the case in real microscopes. We refer to the non-separability of the detection kernel as *spatio-angular coupling* because the orientation of the dipole is coupled to the spatial pattern of irradiance on the detector.

The paraxial detection kernel is rotationally symmetric—it depends on r_d instead of $\mathbf{r}_d$. This symmetry is a result of the $\pi/2$ phase shift between the linear and radial fields on the detector. If the phase shift between the linear and radial fields was not exactly $\pi/2$ then the fields would interfere on the detector, and we would lose rotational symmetry. Tracing back further, the rotational symmetry is due to the fact that the field in the back focal plane could be written as a sum of a linear and radial field which is only true under the paraxial approximation—the

rotational symmetry of the detection kernel is only true to first order. Despite the approximation, we still feel that the rotational symmetry of the detection kernel is a valuable result since it helps build an intuition about the dominant effects outside the paraxial approximation.

Note that we have restricted our analysis to an imaging system with unit magnification. We will continue with this simplification and mention that an imaging system with an arbitrary magnification can be modeled using the model for a system with unit magnification and a change of variable (see [5] section 7.2.7).
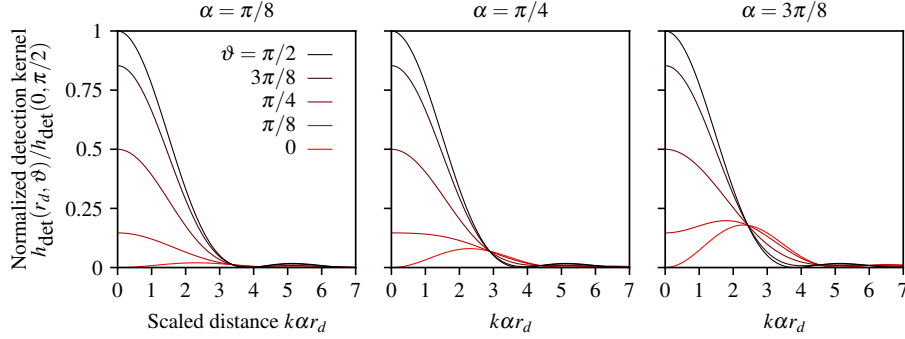
Fig. 8. Normalized detection kernel as a function of the scaled radial detection coordinate $k\alpha r_d$, the dipole inclination angle ϑ, and the collection angle α. For small collection angles (left) the detection kernel of axial dipoles (**red**) is small compared to transverse dipoles (**black**), but the relative contribution of axial dipoles increases with the collection angle (see **red** lines from left to right).

3.2.3. Complete orientation-dependent point spread function

Combining the results of the previous two sections yields a simplified dipole imaging model

$$g(\mathbf{r}_d) = \int_{\mathbb{S}^2} d\hat{\mathbf{s}}_o \int_{\mathbb{R}^2} d\mathbf{r}_o \, h(|\mathbf{r}_d - \mathbf{r}_o|, |\hat{\mathbf{s}}_o \cdot \hat{\mathbf{z}}|) f(\mathbf{r}_o, \hat{\mathbf{s}}_o). \tag{66}$$

where we have written the kernel in terms of $|\hat{\mathbf{s}}_o \cdot \hat{\mathbf{z}}| = \cos\vartheta$ to explicitly show the dependence on $\hat{\mathbf{s}}_o$. In previous sections we showed that the kernel is given by

$$h(r, \vartheta) \propto h_{\text{exc}}(\vartheta) h_{\text{det}}(r, \vartheta). \tag{67}$$

Plugging in our results we find:

$$h(r, \vartheta) \propto \left[\sin^2\vartheta + \frac{1}{2}\alpha^2 \cos^2\vartheta \right] \left[a_1(r) \sin^2\vartheta + \frac{1}{2}\alpha^2 a_2(r) \cos^2\vartheta \right]. \tag{68}$$

Comment on inversion/antipodal symmetry.

To demonstrate the orientation-dependent point spread function, we calculate the irradiance pattern created by a set of equally spaced dipoles with varying orientation given by

$$f_{(\text{ph1})}(x_o, y_o, \vartheta, \varphi) = \sum_{i=0}^{3} \sum_{j=0}^{3} \delta\left(x_o - \frac{i}{3}\right) \delta\left(y_o - \frac{j}{3}\right) \delta\left(\cos\vartheta - \cos\left(\frac{\pi i}{6}\right)\right) \delta\left(\varphi - \frac{2\pi j}{3}\right), \tag{69}$$
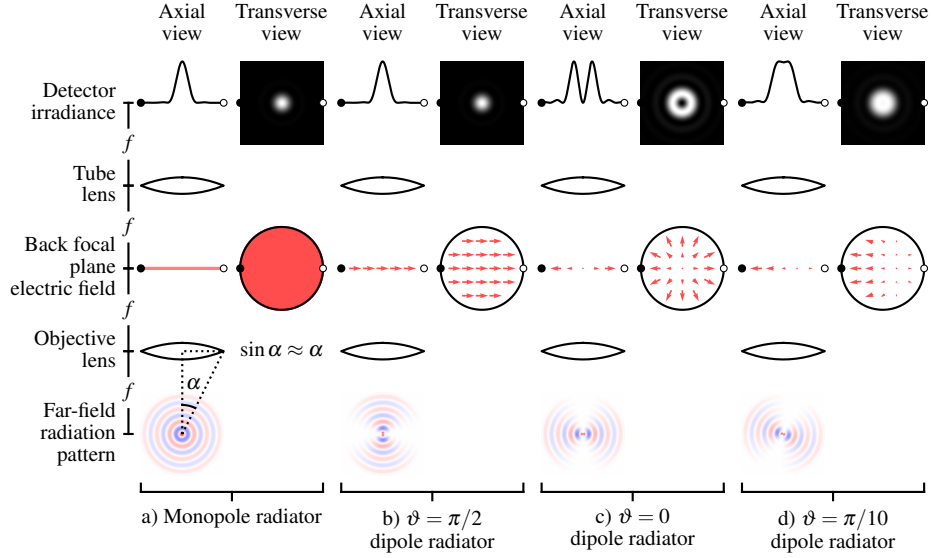
Fig. 9. Comparison of paraxial detection models for monopole radiators a) and dipole radiators b)–d). a) Monopole radiators fill the back focal plane with a uniform scalar field which gives rise to the familiar Airy disk on the detector. b) A transverse dipole radiator also creates an Airy disk, but the back focal plane is filled with a uniform vector field. c) An axial dipole radiator creates a radial electric field pattern in the back focal plane which creates a higher-order Airy disk on the detector. d) Dipoles that are not transverse or axial still create radially symmetric irradiance patterns under the paraxial approximation. Fields from transverse dipoles are real and even while fields from axial dipoles are real and odd which causes a relative $\pi/2$ phase shift for the fields on the detector. This phase shift means that the fields from transverse and axial components of the dipole do not interfere, which causes radially symmetric irradiance patterns.

where the subscript (ph1) indicates that this is the first phantom. To find the irradiance pattern we plug Eq. 69 into Eq. 66 and use the sifting property

$$g_{(\text{ph1})}(x_d, y_d) = \sum_{i=0}^{3} \sum_{j=0}^{3} h\left(\sqrt{\left(x_d - \frac{i}{3}\right)^2 + \left(y_d - \frac{j}{3}\right)^2}, \frac{\pi i}{6} \right). \tag{70}$$

3.3. *Orientation-dependent optical transfer function of a paraxial epi-fluorescence microscope*

In Appendix C we evaluate the 2D spatial Fourier transforms of $a_1(r)$ and $a_2(r)$ to find that

$$H(\nu, \vartheta) \propto \left[\sin^2 \vartheta + \frac{1}{2}\alpha^2 \cos^2 \vartheta \right] \left[A_1(\nu) \sin^2 \vartheta + \frac{1}{2}\alpha^2 A_2(\nu) \cos^2 \vartheta \right]. \tag{71}$$

where

$$A_1(\nu) = \frac{2}{\pi} \left\{ \cos^{-1}\left(\frac{\nu}{2\nu_o}\right) - \frac{\nu}{2\nu_o} \sqrt{1 - \left(\frac{\nu}{2\nu_o}\right)^2} \right\} \Pi\left(\frac{\nu}{4\nu_o}\right), \tag{72}$$

$$A_2(\nu) = \frac{2}{\pi} \left\{ \cos^{-1}\left(\frac{\nu}{2\nu_o}\right) - \left[3 - 2\left(\frac{\nu}{2\nu_o}\right)^2\right] \frac{\nu}{2\nu_o} \sqrt{1 - \left(\frac{\nu}{2\nu_o}\right)^2} \right\} \Pi\left(\frac{\nu}{4\nu_o}\right). \tag{73}$$

The orientation-dependent optical transfer function is shown in Figure 10. The orientation-dependent transfer function has the usual spatial-frequency cutoff at $\nu_c = 2\nu_o$ for all dipole orientations.
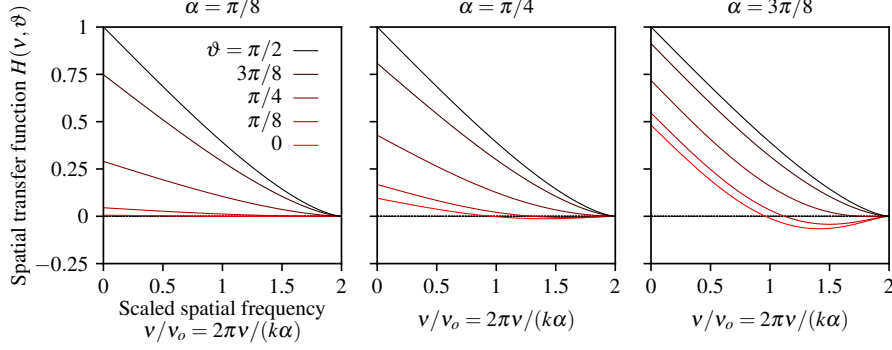

Fig. 10. Orientation-dependent transfer function as a function of the scaled spatial frequency, the dipole inclination angle ϑ, and the collection angle α. For small collection angles (left) the STF for axial dipoles (**red**) is small compared to transverse dipoles (**black**), but the relative contribution of axial dipoles increases with the collection angle (see **red** lines from left to right). The STF of axial dipoles is negative at high spatial frequencies because the central minimum of the axial kernel corresponds to the position of the dipole. Equivalently, a high-spatial-frequency pattern of axial dipoles will generate an irradiance pattern where the minimum irradiance corresponds to the peak of the axial dipole density.

To demonstrate the spatial transfer spread function, we calculate the irradiance pattern created by a set of equally spaced disks with varying radius containing fluorophores with varying orientation given by

$$f_{(\mathrm{ph2})}(x_o, y_o, \vartheta, \varphi) = \sum_{i=0}^{3} \sum_{j=0}^{3} \Pi\left(\frac{10}{j}\sqrt{\left(x_o - \frac{i}{3}\right)^2 + \left(y_o - \frac{j}{3}\right)^2}\right) \delta\left(\cos\vartheta - \cos\left(\frac{\pi i}{6}\right)\right) \delta\left(\varphi - \frac{2\pi j}{3}\right).$$
(74)

$$G_{(\mathrm{ph2})}(\nu_x, \nu_y) = \sum_{i=0}^{3} \sum_{j=0}^{3} H\left(\nu_x, \nu_y, \frac{\pi i}{6}, \frac{2\pi j}{3}\right)\left[\frac{j}{10\nu}J_1\left(\frac{2\pi j\nu}{10}\right)\right]\exp\left(-2\pi i\left[\frac{i}{3}\nu_x + \frac{j}{3}\nu_y\right]\right). \quad (75)$$

Finally, we calculate the inverse Fourier transform of the irradiance spectrum to find the irradiance.

3.4. Angular transfer function (ATF) of a paraxial epi-fluorescence microscope

To calculate the angular transfer function we plug the spatio-angular point spread function Eq. 68 into Eq. 28 and evaluate the integrals using a computer algebra package [12] to find

$$
\begin{aligned}
H_l^m(r) \propto \quad & 7\{ \; 32a_1(r) + 4\alpha^2[a_1(r) + a_2(r)] + 3\alpha^4 a_2(r)\}\delta_{\ell 0}\delta_{m0} + \\
& 4\sqrt{5}\{-16a_1(r) + \; \alpha^2[a_1(r) + a_2(r)] + 3\alpha^4 a_2(r)\}\delta_{\ell 2}\delta_{m0} + \\
& 8\{ \; 4a_1(r) - 2\alpha^2[a_1(r) + a_2(r)] + \; \alpha^4 a_2(r)\}\delta_{\ell 4}\delta_{m0}.
\end{aligned}
$$
(76)

The degree ℓ and order m of the non-zero terms in the ATF follow directly from specific features of the kernel. First, the spatio-angular point spread function is symmetric under inversion of

the dipole moment. This symmetry is maintained in the angular transfer function since all of the non-zero terms have an even degree $\ell = 0, 2, 4$, and the corresponding spherical harmonics $Y_0^0(\hat{\mathbf{s}}_o), Y_2^0(\hat{\mathbf{s}}_o), Y_4^0(\hat{\mathbf{s}}_o)$ are symmetric under inversion. Second, we showed that under the paraxial approximation our kernel is rotationally symmetric which allows us to write the kernel as a function of r instead of $\mathbf{r}$. This symmetry is maintained in the ATF since all of the non-zero terms have order $m = 0$. Finally, both the excitation and detection kernels are degree-2 trigonometric polynomials, which implies that the maximum degree of the spatio-angular point spread function is 4. This feature of the kernel appears in the angular transfer function since only $\ell = 0, 2$, and 4 terms are non-zero.
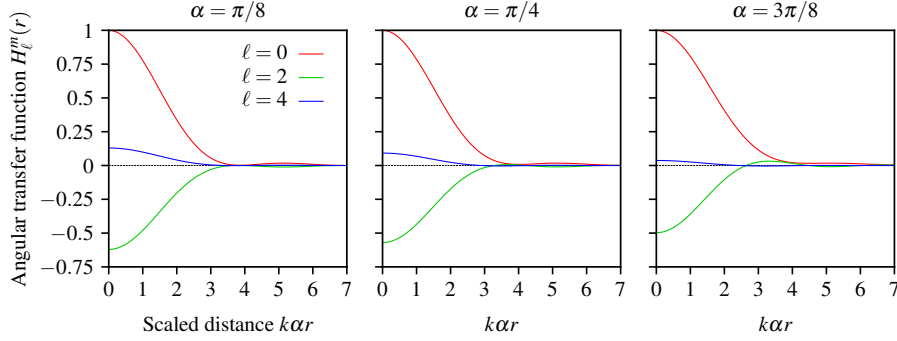

Fig. 11. ATF as a function of the scaled radial detection coordinate $k\alpha r$, the spherical harmonic degree ℓ, and the collection angle α.

To demonstrate the angular transfer function, we calculate the irradiance pattern created by a set of equally spaced fluorophore distributions with varying orientation and angular distribution given by

$$f_{(ph3)}(x_o, y_o, \vartheta, \varphi) = \sum_{i=0}^{3} \sum_{j=0}^{3} \delta\left(x_o - \frac{i}{3}\right) \delta\left(y_o - \frac{j}{3}\right) f_{(cone)}\left(\vartheta, \varphi; \frac{\pi i}{6}, \frac{2\pi j}{3}, \frac{\pi i}{6}\right), \qquad (77)$$

where

$$f_{(cone)}(\hat{\mathbf{s}}_o; \hat{\mathbf{s}}_o', \Delta) = f_{(cone)}(\vartheta, \varphi; \vartheta', \varphi', \Delta) = \frac{1}{4\pi(1 - \cos \Delta)} \Pi\left(\frac{\hat{\mathbf{s}} \cdot \hat{\mathbf{s}}'}{\cos \Delta}\right). \qquad (78)$$

To calculate the irradiance pattern we calculate the angular density spectrum of the phantom (we calculate the spherical Fourier transform of the cone in Appendix D), plug the result into Eq. XXX, then use the sifting property to find that

$$g_{(ph3)}(x_d, y_d) = \sum_{\ell m} \sum_{i=0}^{3} \sum_{j=0}^{3} H_\ell^m\left(\sqrt{\left(x_d - \frac{i}{3}\right)^2 + \left(y_d - \frac{j}{3}\right)^2}\right) F_{\ell(cone)}^m\left(\frac{\pi i}{6}, \frac{2\pi j}{3}, \frac{\pi i}{6}\right), \qquad (79)$$

3.5. Spatio-angular transfer function (SATF) of a paraxial epi-fluorescence microscope

$$\begin{aligned} H_l^m(\nu) \propto \quad & 7\{ \ 32A_1(\nu) + 4\alpha^2[A_1(\nu) + A_2(\nu)] + 3\alpha^4 A_2(\nu)\}\delta_{\ell 0}\delta_{m0} + \\ & 4\sqrt{5}\{-16A_1(\nu) + \ \alpha^2[A_1(\nu) + A_2(\nu)] + 3\alpha^4 A_2(\nu)\}\delta_{\ell 2}\delta_{m0} + \\ & 8\{ \ \ 4A_1(\nu) - 2\alpha^2[A_1(\nu) + A_2(\nu)] + \ \alpha^4 A_2(\nu)\}\delta_{\ell 4}\delta_{m0}. \end{aligned} \qquad (80)$$
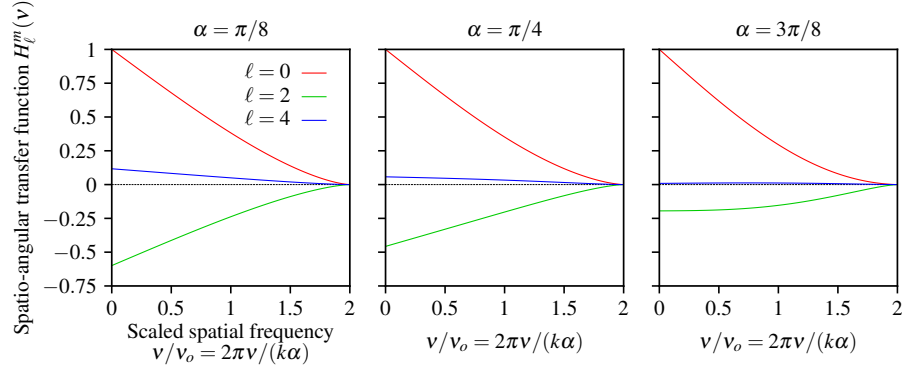
Fig. 12. SATF as a function of the scaled spatial frequency, the spherical harmonic degree ℓ, and the collection angle α.

To demonstrate the spatio-angular transfer function, we calculate the irradiance pattern created by a set of equally spaced disks of fluorophores with varying radius and angular distribution given by

$$f_{(\text{ph4})}(x_o, y_o, \vartheta, \varphi) = \sum_{i=0}^{3} \sum_{j=0}^{3} \Pi \left(\frac{10}{j} \sqrt{\left(x_o - \frac{i}{3}\right)^2 + \left(y_o - \frac{j}{3}\right)^2} \right) f_{(\text{cone})} \left(\vartheta, \varphi; \frac{\pi}{2}, 0, \frac{\pi i}{6} \right), \quad (81)$$

To calculate the irradiance pattern created by the phantom we calculate the spatio-angular spectrum, plug the result into Eq. XXX, then take the inverse Fourier transform to find the irradiance.

$$G_{(\text{ph2})}(\nu_x, \nu_y) = \sum_{\ell m} \sum_{i=0}^{3} \sum_{j=0}^{3} H_\ell^m(\nu_x, \nu_y) \left[\frac{j}{10\nu} J_1 \left(\frac{2\pi j \nu}{10} \right) \right] \exp \left(-2\pi i \left[\frac{i}{3} \nu_x + \frac{j}{3} \nu_y \right] \right) F_{\ell(\text{cone})}^m \left(\frac{\pi i}{6}, \frac{2\pi j}{3}, \frac{\pi i}{6} \right).$$
$$(82)$$

4. Discussion

4.1. Reconstructions

Since the ATF effectively contains three OTFs it is tempting to conclude that fluorescence microscopes pass three times as much information about the dipoles as monopoles. This is not true. The microscope still only measures a single member of $\mathbb{L}_2(\mathbb{R}^2)$, so at best we can recover the same amount of information about the object. In other words, we know immediately that the microscope is a rank-1 operator since it only measures one continuous function.

TODO Expand. Make clear that later paper. We postpone a full discussion of SVD to find the object space singular functions that span the measurement space of the instrument.

4.2. Alternative transfer functions

Throughout this work we have used the spherical harmonic functions as a basis for functions on the sphere, but there are other basis functions that can be advantageous in some cases. Backer and others [CITE TODO] have used the second moments as basis functions for the sphere because they arise naturally when computing the spatio-angular point spread function. Mathematically, Backer and [XXX] use an alternative to the angular transfer function that uses the second moments as

basis functions so their forward model is given by

$$g(\mathbf{r}_d) = \sum_{j=1}^{6} H_j(\mathbf{r}_d - \mathbf{r}_o)F_j(\mathbf{r}_o), \tag{83}$$

where

$$H_j(\mathbf{r}_d - \mathbf{r}_o) = \int_{\mathbb{S}^2} d\hat{\mathbf{s}}_o \, h(\mathbf{r}_d - \mathbf{r}_o, \hat{\mathbf{s}}_o)Z_j(\hat{\mathbf{s}}_o), \tag{84}$$

$$F_j(\mathbf{r}_o) = \int_{\mathbb{S}^2} d\hat{\mathbf{s}}_o \, f(\mathbf{r}_o, \hat{\mathbf{s}}_o)Z_j(\hat{\mathbf{s}}_o), \tag{85}$$

and $Z_j(\hat{\mathbf{s}}) = \{s_x^2, s_y^2, s_z^2, s_x s_y, s_y s_z, s_x s_z\}$ are the second moments. This formulation is similar to the angular transfer function approach because it exploits the spatial sparsity of sample, but it does not require a cumbersome expansion of the spatio-angular point spread function onto spherical harmonics.

However, the spherical harmonics provide several advantages over the second moments. First, the spherical harmonics form a complete basis for functions on the sphere, while the second moments span a much smaller function space. The usual approach to extending the span of the second moments is to use the fourth (or higher) moments, but these are completely new basis functions. Indeed, the microscope we considered in this work cannot be represented using the second moments since it contains fourth-order terms. Second, the spherical harmonics are orthonormal which allows us to easily deploy tools from linear algebra. For example, the spatio-angular transfer function for the microscope we considered in this work required three angular terms so we can think of the angular response as a vector in a three-dimensional vector space. If we had used the second moments we would have required six terms, and we would not have been able to say anything about the dimension of the space since the second moments are not orthonormal. Finally, using the spherical harmonics provides access to a set of fast algorithms. The naive expansion of an arbitrary discretized N point spherical function onto spherical harmonics (or second moments) requires a $\mathcal{O}(N^2)$ matrix multiplication, while pioneering work by Driscoll and Healy [cite] showed that the forward discrete fast spherical harmonic transform can be computed with a $\mathcal{O}(N(\log N)^2)$ algorithm and its inverse can be computed with a $\mathcal{O}(N^{3/2})$ algorithm. To our knowledge no similarly fast algorithms exist for expansion onto the higher-order moments.

4.3. What determines the angular frequency cutoff?

The spatial-frequency cutoff of a fluorescence microscope is well known to vary as NA/λ—we can increase spatial resolution by increasing the NA of the instrument or by choosing a fluorophore with a shorter emission wavelength. Analogously, the angular-frequency spectrum of a fluorescence microscope depends on both the instrument and the sample.

The simple paraxial microscope considered in this work always has three terms in its angular-frequency spectrum, but we can increase the number of terms by modifying the instrument. We will postpone the complete treatment of these effects until future work, but we briefly mention that the number of terms in the angular-frequency spectrum increases for non-paraxial microscopes, microscopes with polarizers on the illumination or detection paths, and multiview microscopes. We also mention that there are two ways to extend the angular-frequency spectrum of a microscope—by increasing the degree ℓ and by increasing the order m. Extending the angular degree cutoff ℓ_c gives the microscope the ability to measure finer angular features, while extending the angular order cutoff m_c give the microscope the ability to measure features of the object that are increasingly invariant to rotation. If the angular order cutoff matches the angular degree cutoff $\ell_c = m_c$ then the microscope can be said to have *isotropic angular resolution*. This

condition is not met by a single-view paraxial microscope since $\ell_0 = 4$ and $m_0 = 0$, but we will model microscopes with this property in future work.

The number of terms in the angular frequency spectrum is also sample dependent. Monopoles emit light isotropically so they have a single term, dipoles have a three-term ATF, and higher-order excitation and detection moments will have even more terms—these objects have different angular band limits. We emphasize the similarity between the spatial and angular frequency cutoffs—both the sample and the instrument affect the maximum achievable resolution of the imaging system.

4.4. Characterizing real spatio-angular microscopes

The theoretical model we present in this work is an extreme simplification of a real microscope. We have ignored the effects of thick samples, optical aberration, scattering, high-NA objectives, finite fluorescence lifetimes, and interactions between fluorophores, among other. Because of this long list of unknown effects, real experiments should make an attempt to characterize the specific imaging system.

Typical fluorescence microscopy experiments start with the monopole approximation and attempt to characterize the microscope by imaging sub-diffraction beads. These images are assumed to be good approximations of the monopole point spread function and this data can be used to restore (deconvolve) the data taken in arbitrary experiments.

Imaging sub-diffraction beads is not enough to completely characterize the response of a microscope to an oriented sample. We need at least three samples with a known orientations to characterize the SATF, so isotropic beads are not enough. Small beads may not be isotropic [cite Lew].

5. Conclusion

Most models of fluorescence microscopes use a monopole model to describe the object and the imaging system. A more complete description of any fluorescence microscope requires a dipole model of the object and a model of the spatio-angular point spread function. We developed several transfer functions that simplify the mapping between the spatio-angular density and the irradiance pattern on the detector, and we demonstrated these transfer functions by efficiently simulating a paraxial widefield fluorescence microscope.

References

1. A. S. Backer and W. E. Moerner, "Extending single-molecule microscopy using optical Fourier processing," J. Phys. Chem. B **118**, 8313–8329 (2014).
2. M. A. Lieb, J. M. Zavislan, and L. Novotny, "Single-molecule orientations determined by direct emission pattern imaging," J. Opt. Soc. Am. B **21**, 1210–1215 (2004).
3. M. P. Backlund, M. D. Lew, A. S. Backer, S. J. Sahl, and W. E. Moerner, "The role of molecular dipole orientation in single-molecule fluorescence microscopy and implications for super-resolution imaging," ChemPhysChem **15**, 587–599 (2014).
4. S. B. Mehta, M. McQuilken, P. J. La Rivière, P. Occhipinti, A. Verma, R. Oldenbourg, A. S. Gladfelter, and T. Tani, "Dissection of molecular assembly dynamics by tracking orientation and position of single molecules in live cells," Proc. Natl. Acad. Sci. U.S.A. **113**, E6352–E6361 (2016).
5. H. Barrett and K. Myers, *Foundations of image science*, Wiley series in pure and applied optics (Wiley-Interscience, 2004).
6. J. T. Fourkas, "Rapid determination of the three-dimensional orientation of single molecules," Opt. Lett. **26**, 211–213 (2001).
7. T. Chandler, S. Mehta, H. Shroff, R. Oldenbourg, and P. J. La Rivière, "Single-fluorophore orientation determination with multiview polarized illumination: modeling and microscope design," Opt. Express **25**, 31309–31325 (2017).
8. M. R. Foreman and P. Török, "Computational methods in vectorial imaging," J. Mod. Opt. **58**, 339–364 (2011).
9. L. Novotny and B. Hecht, *Principles of Nano-Optics* (Cambridge University Press, 2006).
10. A. Agrawal, S. Quirin, G. Grover, and R. Piestun, "Limits of 3D dipole localization and orientation estimation for single-molecule imaging: towards Green's tensor engineering," Opt. Express **20**, 26667–26680 (2012).
11. J. Goodman, *Introduction to Fourier Optics* (McGraw-Hill, 1996), 2nd ed.

12. A. Meurer, C. P. Smith, M. Paprocki, O. Čertík, S. B. Kirpichev, M. Rocklin, A. Kumar, S. Ivanov, J. K. Moore, S. Singh, T. Rathnayake, S. Vig, B. E. Granger, R. P. Muller, F. Bonazzi, H. Gupta, S. Vats, F. Johansson, F. Pedregosa, M. J. Curry, A. R. Terrel, v. Roučka, A. Saboo, I. Fernando, S. Kulal, R. Cimrman, and A. Scopatz, "SymPy: symbolic computing in Python," PeerJ Comput. Sci. **3**, e103 (2017).

13. N. Schaeffer, "Efficient spherical harmonic transforms aimed at pseudospectral numerical simulations," Geochem. Geophys. Geosystems **14**, 751–758 (2013).

14. J. Mertz, *Introduction to Optical Microscopy* (W. H. Freeman, 2009).

15. I. S. Gradshteyn and I. M. Ryzhik, *Table of integrals, series, and products* (Elsevier/Academic Press, Amsterdam, 2007), seventh ed. Translated from the Russian, Translation edited and with a preface by Alan Jeffrey and Daniel Zwillinger, With one CD-ROM (Windows, Macintosh and UNIX).

A. Fourier transform of linear and radial vector fields

In this appendix we evaluate the two-dimensional Fourier transform of the electric field in the back focal plane of paraxial epi-fluorescence microscope given by

$$\mathbf{E}_{\text{det}}(\mathbf{r}_d, \hat{\mathbf{s}}_o) = \int_{\mathbb{R}^2} d\mathbf{r}_b \mathbf{E}_{\text{bfp}}(\mathbf{r}_b) \exp\left[ik\, \mathbf{r}_b \cdot \mathbf{r}_d\right], \tag{86}$$

where

$$\mathbf{E}_{\text{bfp}}(r_b, \phi_b, \hat{\mathbf{s}}_o) \propto \left\{ s_x \hat{\mathbf{x}} + s_y \hat{\mathbf{y}} - s_z r_b \hat{\boldsymbol{\rho}} \right\} \Pi\left(\frac{r_b}{\alpha}\right). \tag{87}$$

To evaluate the Fourier transform we rewrite it in polar coordinates

$$\mathbf{E}_{\text{det}}(\mathbf{r}_d, \hat{\mathbf{s}}_o) = \int_0^\infty r_b dr_b \int_0^{2\pi} d\phi_b \, \mathbf{E}_{\text{bfp}}(r_b, \phi_b) \exp\left[ikr_b r_d \cos(\phi_b - \phi_d)\right], \tag{88}$$

plug in Eq. 87, and apply the following pair of identities

$$\int_0^{2\pi} d\phi_b \left\{ \begin{matrix} \sin(n\phi_b) \\ \cos(n\phi_b) \end{matrix} \right\} \exp\left[ikr_b r_d \cos(\phi_b - \phi_d)\right] = 2\pi i^n \left\{ \begin{matrix} \sin(n\phi_d) \\ \cos(n\phi_d) \end{matrix} \right\} J_n(kr_b r_d), \tag{89}$$

and

$$\int_0^\alpha dr_b (r_b)^{n+1} J_n(kr_b r_d) = \alpha^{n+1} \left[\frac{J_{n+1}(k\alpha r_d)}{kr_d}\right], \tag{90}$$

to find that

$$\mathbf{E}_{\text{det}}(\mathbf{r}_d, \hat{\mathbf{s}}_o) \propto \left[s_x \frac{J_1(k\alpha r_d)}{k\alpha r_d} - i s_z \alpha \frac{J_2(k\alpha r_d)}{k\alpha r_d} \cos\phi_d \right] \hat{\mathbf{x}} +$$
$$\left[s_y \frac{J_1(k\alpha r_d)}{k\alpha r_d} - i s_z \alpha \frac{J_2(k\alpha r_d)}{k\alpha r_d} \sin\phi_d \right] \hat{\mathbf{y}}. \tag{91}$$

Similar to the expression for the electric field in the back focal plane, we rewrite Eq. 91 in terms of linear and radial vector fields

$$\mathbf{E}_{\text{det}}(\mathbf{r}_d, \hat{\mathbf{s}}_o) \propto \frac{J_1(k\alpha r_d)}{k\alpha r_d}[s_x \hat{\mathbf{x}} + s_y \hat{\mathbf{y}}] - i\alpha \frac{J_2(k\alpha r_d)}{k\alpha r_d} s_z \hat{\boldsymbol{\rho}}. \tag{92}$$

B. Spherical harmonics

The spherical harmonic function of degree ℓ and order $-\ell \le m \le \ell$ is defined as [13]

$$Y_\ell^m(\vartheta, \varphi) = \sqrt{\frac{2\ell + 1}{4\pi}} \sqrt{\frac{(\ell - |m|)!}{(\ell + |m|)!}} P_\ell^m(\cos\vartheta) \exp(im\varphi), \tag{93}$$

where $P_\ell^m(\cos\theta)$ are the associated Legendre polynomials with the Condon-Shortley phase

$$P_\ell^m(x) = (-1)^m (1-x^2)^{|m|/2} \frac{d^{|m|}}{dx^{|m|}} P_\ell(x), \tag{94}$$

and $P_\ell(x)$ are the Legendre polynomials defined by the recurrence

$$P_0(x) = 1, \tag{95}$$
$$P_1(x) = x, \tag{96}$$
$$\ell P_\ell(x) = (2\ell - 1)x P_{\ell-1}(x) - (\ell - 1)P_{\ell-2}(x). \tag{97}$$

The spherical harmonics are orthonormal, which means that

$$\int_{\mathbb{S}^2} d\hat{\mathbf{s}}\, Y_\ell^m(\hat{\mathbf{s}}) Y_{\ell'}^{m'*}(\hat{\mathbf{s}}) = \delta_{\ell\ell'}\delta_{mm'}, \tag{98}$$

where $\delta_{\ell\ell'}$ denotes the Kronecker delta. The spherical harmonics form a complete basis so an arbitrary function on the sphere $f(\hat{\mathbf{s}})$ can be expanded into a sum of weighted spherical harmonic functions

$$f(\hat{\mathbf{s}}) = \sum_{\ell=0}^{\infty} \sum_{m=-\ell}^{l} F_\ell^m Y_\ell^m(\hat{\mathbf{s}}). \tag{99}$$

We can find the spherical harmonic coefficients F_ℓ^m for a given function using Fourier's trick—multiply both sides by $\bar{Y}_\ell^m(\hat{\mathbf{s}})$, integrate over the sphere, and exploit orthogonality to find that

$$F_\ell^m = \int_{\mathbb{S}^2} d\hat{\mathbf{s}}\, f(\hat{\mathbf{s}}) \bar{Y}_\ell^m(\hat{\mathbf{s}}). \tag{100}$$

The coefficients F_ℓ^m are called the *spherical Fourier transform* of a spherical function.

We briefly show how two properties of spherical functions propagate to the spherical Fourier transform. First, the spherical harmonic coefficients of spherical functions that can be written entirely as a function of the inclination angle ϑ are zero when $m \neq 0$ because

$$\int_{\mathbb{S}^2} d\hat{\mathbf{s}}\, f(\vartheta) \bar{Y}_\ell^m(\hat{\mathbf{s}}) = \int_0^{2\pi} d\phi \exp[-im\varphi] \int_0^{\pi} d\vartheta\, \sin\vartheta f(\vartheta) P_\ell^m(\cos\vartheta), \tag{101}$$

$$= \delta_{m0} \int_0^{\pi} d\vartheta\, \sin\vartheta f(\vartheta) P_\ell^m(\cos\vartheta). \tag{102}$$

Second, the spherical harmonic coefficients of spherical functions that are symmetric under inversion $f(\hat{\mathbf{s}}) = f(-\hat{\mathbf{s}})$ are zero when ℓ is odd because $Y_\ell^m(-\hat{\mathbf{s}}_o) = (-1)^\ell Y_\ell^m(\hat{\mathbf{s}})$, so if ℓ is odd then

$$\int_{\mathbb{S}^2} d\hat{\mathbf{s}}\, f(\hat{\mathbf{s}}) \bar{Y}_{2n+1}^m(\hat{\mathbf{s}}) = \int_{\mathbb{S}^2/2} d\hat{\mathbf{s}}\, f(+\hat{\mathbf{s}}) \bar{Y}_{2n+1}^m(+\hat{\mathbf{s}}) + \int_{\mathbb{S}^2/2} d\hat{\mathbf{s}}\, f(-\hat{\mathbf{s}}) \bar{Y}_{2n+1}^m(-\hat{\mathbf{s}}), \tag{103}$$

$$= \int_{\mathbb{S}^2/2} d\hat{\mathbf{s}}\, f(\hat{\mathbf{s}}) \bar{Y}_{2n+1}^m(+\hat{\mathbf{s}}) - \int_{\mathbb{S}^2/2} d\hat{\mathbf{s}}\, f(\hat{\mathbf{s}}) \bar{Y}_{2n+1}^m(\hat{\mathbf{s}}) = 0. \tag{104}$$

C. Fourier transform of higher-order Airy patterns

In this appendix we will evaluate the two-dimensional Fourier transform of the higher-order Airy patterns given by

$$A_n(\boldsymbol{v}) = \int_{\mathbb{R}^2} d\mathbf{r}\, a_n(\mathbf{r}) \exp\left[-2\pi i \mathbf{r} \cdot \boldsymbol{v}\right], \tag{105}$$

where

$$a_n(\mathbf{r}) = \frac{n}{\pi} \left[\frac{J_n(k\alpha r)}{r} \right]^2 . \tag{106}$$

The crucial step is to rewrite the function $a_n(\mathbf{r})$ in terms of the absolute square of a simpler function with a known Fourier transform. In this case we rewrite as

$$A_n(\boldsymbol{\nu}) = \frac{n}{\pi} \int_{\mathbb{R}^2} d\mathbf{r} \, |t(\mathbf{r})|^2 \exp\left[-2\pi i \mathbf{r} \cdot \boldsymbol{\nu}\right], \tag{107}$$

where

$$t_n(\mathbf{r}) = \frac{J_n(2\pi \nu_o r)}{r} \exp[i(n-1)\phi]. \tag{108}$$

where $2\pi \nu_o = k\alpha$. Note that we have made a non-obvious choice for $t_n(\mathbf{r})$ because we know that we can find its Fourier transform.

Now we can apply the autocorrelation theorem to rewrite the Fourier transform as

$$A_n(\boldsymbol{\nu}) = \frac{n}{\pi} \int_{\mathbb{R}^2} d\boldsymbol{\tau} \, T_n(\boldsymbol{\tau}) \bar{T}_n(\boldsymbol{\tau} - \boldsymbol{\nu}), \tag{109}$$

where

$$T_n(\boldsymbol{\tau}) = \int_{\mathbb{R}^2} d\mathbf{r} \, t_n(\mathbf{r}) \exp\left[-2\pi i \mathbf{r} \cdot \boldsymbol{\tau}\right]. \tag{110}$$

We can evaluate $T_n(\boldsymbol{\tau})$ by rewriting in polar coordinates

$$T_n(\boldsymbol{\tau}) = \int_0^{2\pi} d\phi \int_0^\infty dr \, J_n(2\pi \nu_o r) \exp[i(n-1)\phi] \exp\left[2\pi i r \tau \cos(\phi - \phi_\tau)\right]. \tag{111}$$

then evaluating the integrals with the identities (Barrett 4.111)

$$\int_0^{2\pi} d\phi \exp[i(n-1)\phi] \exp[2\pi i \tau r \cos(\phi - \phi_\tau)] = 2\pi i^{n-1} \exp[i(n-1)\phi_\tau] J_{n-1}(2\pi \tau r). \tag{112}$$

and (GR 6.162)

$$\int_0^\infty dr \, J_n(2\pi \nu_o r) J_{n-1}(2\pi \tau r) = \frac{1}{2\pi} \frac{\tau^{n-1}}{\nu_o^n} \Pi\left(\frac{\tau}{2\nu_o}\right), \tag{113}$$

which results in

$$T_n(\boldsymbol{\tau}) = \frac{(i\tau \exp[i\phi_\tau])^{n-1}}{\nu_o^n} \Pi\left(\frac{\tau}{2\nu_o}\right). \tag{114}$$

It will be more convenient to set up the autocorrelation in Cartesian coordinates

$$T_n(\boldsymbol{\tau}) = \frac{(i\tau_x - \tau_y)^{n-1}}{\nu_o^n} \Pi\left(\frac{\sqrt{\tau_x^2 + \tau_y^2}}{2\nu_o}\right). \tag{115}$$

Now we can use Eq. 115 to evaluate Eq. 109. Since the autocorrelation is rotationally symmetric we can restrict ourselves to shifts along the $\hat{\mathbf{x}}$ axis so

$$A_n(\nu) = \frac{n}{\pi} \int_{\mathbb{R}^2} d\boldsymbol{\tau} \, T_n(\boldsymbol{\tau}) \bar{T}_n(\boldsymbol{\tau} - \nu \hat{\mathbf{x}}). \tag{116}$$

Plugging in Eq. 115 gives

$$A_n(v) = \frac{n}{\pi v_0^{2n}} \int_{\mathbb{R}^2} d\tau \, (\tau_x^2 + \tau_y^2 - v\tau_x)^{n-1} \Pi\left(\frac{\sqrt{\tau_x^2 + \tau_y^2}}{v_o}\right) \Pi\left(\frac{\sqrt{(\tau_x - v)^2 + \tau_y^2}}{2v_o}\right). \tag{117}$$

We can interpret the autocorrelation as an integral over a region of overlap between a circle centered at the origin and a circle shifted to the right by v (a geometric lens). Using the construction in Figure 13 we can express this region as

$$A_n(v) = \frac{4n}{\pi v_o^{2n}} \left[\int_0^{v_o} \tau d\tau \int_0^{\cos^{-1}\left(\frac{v}{2v_o}\right)} d\phi_\tau (\tau^2 - v\tau \cos\phi_\tau)^{n-1} - \right.$$
$$\left. \int_0^{v/2} d\tau_x \int_0^{\tau_x \frac{2v_o}{v}\sqrt{1-\left(\frac{v}{2v_o}\right)^2}} d\tau_y (\tau_x^2 + \tau_y^2 - v\tau_x)^{n-1} \right] \Pi\left(\frac{v}{4v_o}\right). \tag{118}$$
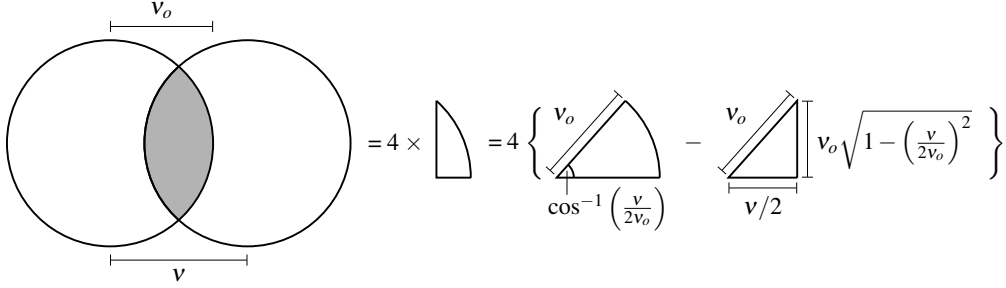

Fig. 13. Geometric construction for evaluating the autocorrelation. We need to integrate over the overlapping region of two circles with radius v_o and distance v between their centers. The region is given by four times the difference in area between a sector of angle $\arccos\left(\frac{v}{2v_o}\right)$ and a triangle with base $v/2$ and hypotenuse v_o.

We will only evaluate these integrals for $n = 1$ and $n = 2$, but the result for arbitrary n is likely possible as a recurrence relation. For $n = 1$:

$$A_1(v) = \frac{4}{\pi v_o^2} \left[\int_0^{v_o} \tau d\tau \int_0^{\cos^{-1}\left(\frac{v}{2v_o}\right)} d\phi_\tau - \int_0^{v/2} d\tau_x \int_0^{\tau_x \frac{2v_o}{v}\sqrt{1-\left(\frac{v}{2v_o}\right)^2}} d\tau_y \right] \Pi\left(\frac{v}{4v_o}\right), \tag{119}$$

$$A_1(v) = \frac{2}{\pi} \left\{ \cos^{-1}\left(\frac{v}{2v_o}\right) - \frac{v}{2v_o}\sqrt{1 - \left(\frac{v}{2v_o}\right)^2} \right\} \Pi\left(\frac{v}{2v_o}\right). \tag{120}$$

which is a well-known result [11, 14]. For $n = 2$:

$$A_2(\nu) = \frac{8}{\pi \nu_o^4} \left[\int_0^{\nu_o} \tau d\tau \int_0^{\cos^{-1}\left(\frac{\nu}{2\nu_o}\right)} d\phi_\tau (\tau^2 - \nu\tau \cos \phi_\tau) - \right. \tag{121}$$

$$\left. \int_0^{\nu/2} d\tau_x \int_0^{\tau_x \frac{2\nu_o}{\nu} \sqrt{1-\left(\frac{\nu}{2\nu_o}\right)^2}} d\tau_y \, (\tau_x^2 + \tau_y^2 - \nu\tau_x) \right] \Pi \left(\frac{\nu}{2\nu_o} \right), \tag{122}$$

$$A_2(\nu) = \frac{2}{\pi} \left\{ \cos^{-1}\left(\frac{\nu}{2\nu_o} \right) - \left[3 - 2\left(\frac{\nu}{2\nu_o} \right)^2 \right] \frac{\nu}{2\nu_o} \sqrt{1 - \left(\frac{\nu}{2\nu_o} \right)^2} \right\} \Pi \left(\frac{\nu}{4\nu_o} \right). \tag{123}$$

D. Spherical Fourier transform of a double cone

In this appendix we will evaluate the spherical Fourier transform of a normalized double-cone angular distribution with central direction $\hat{\mathbf{s}}'$ and cone half-angle Δ

$$f_{(\text{cone})}(\hat{\mathbf{s}}; \hat{\mathbf{s}}', \Delta) = \frac{1}{2\pi(1 - \cos \Delta)} \Pi \left(\frac{\hat{\mathbf{s}} \cdot \hat{\mathbf{s}}'}{\cos \Delta} \right). \tag{124}$$

The spherical Fourier transform is given by

$$F_{\ell(\text{cone})}^m(\hat{\mathbf{s}}', \Delta) = \int_{\mathbb{S}^2} d\hat{\mathbf{s}} \, f_{(\text{cone})}(\hat{\mathbf{s}}; \hat{\mathbf{s}}', \Delta) \bar{Y}_\ell^m(\hat{\mathbf{s}}). \tag{125}$$

The limits of integration will be difficult to find unless we change coordinates to exploit the axis of symmetry $\hat{\mathbf{s}}'$. Since the spherical function is rotationally symmetric about $\hat{\mathbf{s}}'$ we can rotate the function so that the axis of symmetry is aligned with $\hat{\mathbf{z}}$ and multiply by $\sqrt{\frac{4\pi}{2l+1}} Y_\ell^m(\hat{\mathbf{s}}')$ to account for the rotation

$$F_{\ell(\text{cone})}^m(\hat{\mathbf{s}}', \Delta) = \sqrt{\frac{4\pi}{2l+1}} Y_\ell^m(\hat{\mathbf{s}}') \int_{\mathbb{S}^2} d\hat{\mathbf{s}} \, f_{(\text{cone})}(\vartheta; \hat{\mathbf{z}}, \Delta) Y_\ell^0(\hat{\mathbf{s}}). \tag{126}$$

In this coordinate system the double cone is independent of the azimuthal angle, so we can evaluate the azimuthal integral and express the function in terms of an integral over ϑ

$$F_{\ell(\text{cone})}^m(\hat{\mathbf{s}}', \Delta) = 2\pi Y_\ell^m(\hat{\mathbf{s}}') \int_0^\pi d\vartheta \, \sin \vartheta f_{(\text{cone})}(\vartheta; \hat{\mathbf{z}}, \Delta) P_\ell(\cos \vartheta). \tag{127}$$

The function $f_{(\text{cone})}(\vartheta; \hat{\mathbf{z}}, \Delta)$ is only non-zero on the intervals $\vartheta \in [0, \Delta]$ and $\vartheta \in [\pi - \Delta, \pi]$ so

$$F_{\ell(\text{cone})}^m(\hat{\mathbf{s}}', \Delta) = \frac{Y_\ell^m(\hat{\mathbf{s}}')}{2(1 - \cos \Delta)} \left[\int_0^\Delta d\vartheta \, \sin \vartheta P_\ell(\cos \vartheta) + \int_{\pi-\Delta}^\pi d\vartheta \, \sin \vartheta P_\ell(\cos \vartheta) \right]. \tag{128}$$

Applying a change of coordinates with $u = \cos \vartheta$ yields

$$F_{\ell(\text{cone})}^m(\hat{\mathbf{s}}', \Delta) = \frac{Y_\ell^m(\hat{\mathbf{s}}')}{2(1 - \cos \Delta)} \left[\int_{\cos \Delta}^1 d\vartheta \, P_\ell(u) + \int_{-1}^{-\cos \Delta} d\vartheta \, P_\ell(u) \right]. \tag{129}$$

The Legendre polynomials $P_\ell(u)$ are even (odd) on the interval [-1, 1] when ℓ is even (odd), so the pair of integrals will be identical when ℓ is even and cancel when ℓ is odd. For even ℓ

$$F_{\ell(\text{cone})}^m(\hat{\mathbf{s}}', \Delta) = \frac{Y_\ell^m(\hat{\mathbf{s}}')}{1 - \cos \Delta} \int_{\cos \Delta}^1 d\vartheta \, P_\ell(u). \tag{130}$$

The integral evaluates to [15] 7.111

$$\int_{\cos\Delta}^{1} d\vartheta\, P_\ell(u) = \begin{cases} 1 - \cos\Delta, & \ell = 0, \\ \sin\Delta\, P_l^{-1}(\cos\Delta), & \text{else,} \end{cases} \tag{131}$$

where $P_l^{-1}(\cos\Delta)$ is the associated Legendre polynomial with order $m = -1$, not an inverse Legendre polynomial. Bringing everything together

$$F_{\ell(\text{cone})}^m(\hat{\mathbf{s}}', \Delta) = \begin{cases} 1, & \ell = 0, \\ 0, & \ell \text{ odd}, \\ Y_\ell^m(\hat{\mathbf{s}}') \cot\left(\frac{\Delta}{2}\right) P_l^{-1}(\cos\Delta), & \ell > 0 \text{ even}. \end{cases} \tag{132}$$